Copyright

by

Craig Daniel Schindewolf

2022

The Dissertation Committee for Craig Schindewolf certifies that this is the approved version of the following dissertation:

Subversion of innate antiviral immunity by SARS-CoV-2: An example from the study of nonstructural protein 16.

Committee:

Vineet D. Menachery, PhD,
Mentor

Janice J. Endsley, PhD

Shinji Makino, PhD, DVM

Ricardo Rajsbaum, PhD

Matthew D. Daugherty, PhD

Dean, Graduate School

Subversion of innate antiviral immunity by SARS-CoV-2: An example from the study of nonstructural protein 16.

by

Craig D. Schindewolf, BS, MS

Dissertation

Presented to the Faculty of the Graduate School of

The University of Texas Medical Branch

in Partial Fulfillment

of the Requirements

for the Degree of

Doctor of Philosophy in Microbiology and Immunology

The University of Texas Medical Branch

November 3, 2022

Dedication

To all who helped me along the way, professionally and personally. This work was only possible because of the many sacrifices you have made.

Acknowledgements

I thank all the people who had a hand in this work. I especially thank Prof. Vineet Menachery for welcoming me into his laboratory and providing the scientific expertise, equipment, and materials that were foundational to this work, as well as for providing professional guidance. I thank the members of the Menachery Laboratory: Dr. Kumari Lokugamage, Prof. Bryan Johnson, Michelle Vu, Elias Alvarado, and Dr. Birte Kalveram. Each of you played a critical role in moving different experimental aspects of the project forward. Thank you for making the laboratory a collaborative and collegial environment. I also thank former laboratory member Eileen McAnarney for her prior contributions to the laboratory, which facilitated this work.

I also thank the many other scientists at University of Texas Medical Branch that helped with this work: Dionna Scharton, Dr. Jessica Plante, Prof. Ken Plante, and Jordyn Walker of Prof. Scott Weaver's laboratory and the World Reference Center for Emerging Viruses and Arboviruses for help with the most technically challenging aspects of the project *in vivo*. I thank Patricia Crocquet-Valdes and Prof. David Walker for their expertise in histological analysis. I thank Dr. Stephanea Sotcheff, Dr. Elizabeth Jaworski, and Prof. Andrew Routh for help with deep sequencing. I thank Prof. Kari Debbink for help with structural modeling, and Prof. Matthew Daugherty for help with gene silencing and overall project guidance. I thank Gabriel Haila for help with the cell viability assay. I also thank the Institute for Human Infections and Immunity at UTMB for providing a pilot grant to me that helped fund this work.

Lastly, but not least, I would like to thank all the members of my family and community, as well as my fellow UTMB colleagues, for their support while this project was underway. I especially thank my wife, Julianne, for helping me shoulder this project.

Subversion of innate antiviral immunity by SARS-CoV-2: An example from the study of nonstructural protein 16.

Publication No._____

Craig D. Schindewolf, PhD

The University of Texas Medical Branch, 2022

Supervisor: Vineet D. Menachery

Understanding the molecular basis of innate immune evasion by severe acute respiratory syndrome coronavirus 2 (SARS-CoV-2) is an important consideration for designing the next wave of therapeutics. Here, we investigate the role of the nonstructural protein (NSP) 16 of SARS-CoV-2 in infection and pathogenesis. NSP16, a ribonucleoside 2'-O methyltransferase (MTase), catalyzes the transfer of a methyl group to mRNA as part of the capping process. Based on observations with other CoVs, we hypothesized that NSP16 2'-*O* MTase function protects SARS-CoV-2 from cap-sensing host restriction. Therefore, we engineered SARS-CoV-2 with a mutation that disrupts a conserved residue in the active site of NSP16. We subsequently show that this mutant is attenuated both *in vitro* and *in vivo*, using a hamster model of SARS-CoV-2 infection. Mechanistically, we confirm that the NSP16 mutant is more sensitive to type I interferon (IFN-I) *in vitro*. Furthermore, silencing IFIT1 or IFIT3, IFN-stimulated genes that sense a lack of 2'-*O* methylation, partially restores fitness to the NSP16 mutant. Conversely, overexpressing IFIT1 either alone or in combination with IFIT3 attenuates the NSP16 mutant relative to wild-type. Finally, we demonstrate that sinefungin, a MTase inhibitor that binds the catalytic site of NSP16, sensitizes wild-type SARS-CoV-2 to IFN-I treatment and

attenuates viral replication in IFN-I competent cells. Overall, our findings highlight the importance of SARS-CoV-2 NSP16 to evading host innate immunity and suggest a possible target for future antiviral therapies.

Chapters 1, 2, 3, and 4 are based on a manuscript in preparation, which has been made accessible on BioRxiv (*1*):

Schindewolf C, Lokugamage K, Vu MN, Johnson BA, Scharton D, Plante JA, Kalveram B, Crocquet-Valdes PA, Sotcheff S, Jaworski E, Alvarado RE, Debbink K, Daugherty MD, Weaver SC, Routh AL, Walker DH, Plante KS, Menachery VD (2022): "SARS-CoV-2 Uses Nonstructural Protein 16 to Evade Restriction by IFIT1 and IFIT3." *bioRxiv*, 2022.09.26.509529.

TABLE OF CONTENTS

List of Tables x

List of Figures xi

List of Abbreviations xiii

Chapter 1 Introduction – An Overview of Viral Dependence on 2'-*O* Methylation .1

CoV Emergence in the 21st Century 1
CoV Replication and the Nonstructural Proteins.....3
CoV NSP16 and Viral RNA Capping.....5
2'-*O* Methylation in CoVs 7
The Innate Antiviral Response to CoV Infection 7
The IFIT Family.....9
Models of CoV NSP16 MTase Mutant Attenuation.....10
2'-*O* Methylation in Other Virus Families.....14
Summary 15

Chapter 2 Materials and Methods 16

Cell Lines 16
Viruses 16
Viral Replication Kinetics.....20
Plaque Assay 20
Animal Studies.....21
Histology.....21
RNA Purification 22
Sanger Sequencing.....22
Gene Expression via Quantitative PCR (qPCR).....22
DsiRNA Experiments 23
Protein Expression via Western Blot 23
Overexpression of IFIT Proteins.....24
Viability Assay.....24

NSP10 Peptide Design 25
Plaque-Reduction Neutralization Test 25
Morpholino Design and Treatment 25
Statistics 26

Chapter 3 SARS-CoV-2 Uses Nonstructural Protein 16 to Evade Restriction by IFIT1 and IFIT3 30

dNSP16 Has No Replication Defect 30
dNSP16 is Attenuated in Human Respiratory Cells 34
dNSP16 is More Sensitive to IFN-I Pre-Treatment 34
dNSP16 is Attenuated *In Vivo* 36
dNSP16 Replication is Reduced *In Vivo* 40
Knockdown of IFIT Genes Partially Reverses Attenuation of dNSP16 ..43
Overexpression of IFIT1 Results in Attenuation of dNSP16, which is Augmented by Overexpression of IFIT3 50
Targeting the NSP16 Active Site For Antiviral Treatment 52

Chapter 4 Discussion and Future Directions 56

Discussion 56
Future Directions: Targeting NSP16 MTase Function 59
NSP16-Deficiency as a Basis for Live Attenuated Vaccines 66
Exploring Other Roles of NSP16 69

Appendix: Anti-IFIT1 Treatment *In Vivo* 70

Treatment with an Anti-IFIT1 Morpholino in Hamster Differentially Affects Replication of dNSP16 and WT 70

References 76

Vita 86

List of Tables

Table 2.1: Primers used for amplifying hamster targets. 27

Table 2.2: Primers used for amplifying targets in Vero E6 cells. 28

Table 2.3: Dicer-substrate short interfering RNAs (DsiRNAs) used for gene expression knockdown. 29

List of Figures

Figure 1.1: RNA Capping Model in CoVs.....6

Figure 1.2: Alternative Models of CoV NSP16 MTase mutant attenuation. 12

Figure 2.1: General overview of construction of NSP16-mutant SARS-CoV-2 ("dNSP16").....18

Figure 3.1: dNSP16 has no replication defect.....31

Figure 3.2: D130 mutation is stable in rescued dNSP16, and rescued infectious clone stocks maintain sequence around furin cleavage site.....33

Figure 3.3: dNSP16 is attenuated in human respiratory cells and is more sensitive to type I interferon (IFN-I) pre-treatment. 35

Figure 3.4: dNSP16 is attenuated *in vivo*. 37

Figure 3.5: dNSP16 does not drive increased immune gene expression relative to WT. 39

Figure 3.6: dNSP16 replication is reduced *in vivo*.....41

Figure 3.7: No evidence of reversion of dNSP16 mutation was detected *in vivo*...42

Figure 3.8: Knockdown of IFIT genes partially reverses attenuation of dNSP16. .45

Figure 3.9: Validation of knockdown of immune gene targets in Vero E6 cells. ...47

Figure 3.10: Knockdown of either IFIT1 or IFIT3 is specific. 48

Figure 3.11: Overexpression of IFIT1 results in attenuation of dNSP16, which is augmented by overexpression of IFIT3. 51

Figure 3.12: Targeting the NSP16 active site for antiviral treatment. 54

Figure 4.1: WT SARS-CoV-2 replication is reduced by treatment with NSP10 peptide relative to a scrambled control peptide. 65

Figure 4.2: dNSP16 induces serum neutralizing antibody at 7 days post-infection68

Figure A.1: Designing an IFIT1-targeting morpholino for use *in vivo*. 72

Figure A.2: Treatment with an anti-IFIT1 morpholino in hamster differentially affects replication of dNSP16 and WT. 74

List of Abbreviations

SARS-CoV-2	severe acute respiratory syndrome coronavirus 2
CoV	coronavirus
NSP	(coronavirus) nonstructural protein
2'-*O*	oxygen atom bonded to the 2' carbon of ribose
MTase	methyltransferase
IFN-I	type I interferon
SARS-CoV	severe acute respiratory syndrome coronavirus
MERS-CoV	Middle East respiratory syndrome coronavirus
RTC	replication-transcription complex
DMV	double-membrane vesicle
PRR	pattern recognition receptor
ORF	open reading frame
ACE2	angiotensin converting enzyme 2
DPP4	dipeptidyl peptidase 4
ER	endoplasmic reticulum
PRR	pattern recognition receptor
MDA5	melanoma differentiation-associated protein 5
IFIT	interferon-induced protein with tetratricopeptide repeats
NiRAN	nidovirus RNA-dependent RNA polymerase-associated nucleotidyltransferase
MHV	mouse hepatitis virus
KDKE	lysine-aspartic acid-lysine-glutamic acid motif

PAMP	pathogen-associated molecular pattern
ds	double-stranded
TLR	Toll-like receptor
RIG-I	retinoic acid-inducible gene I
RLR	RIG-I-like receptor
NF-κB	nuclear factor κB
eIF	eukaryotic initiation factor
STING	stimulator of interferon genes
IRF	interferon regulatory factor
BMDM	bone marrow-derived macrophage
ISG	interferon-stimulated gene
NS5	(flavivirus) nonstructural protein 5
guanine-N7	nitrogen atom at the 7 position of guanine
dNSP16	NSP16-D130A icSARS-CoV-2, created for this study
WT	icSARS-CoV-2, based on USA/WA1/2020, created for this study
DMEM	Dulbecco's Modified Eagle Medium
FBS	fetal bovine serum
BHK	baby hamster kidney
PCR	polymerase chain reaction
bp	base pair
ic	infectious clone
NCBI	National Center for Biotechnology Information
DPBS	Dulbecco's phosphate-buffered saline, without calcium chloride and magnesium

MOI	multiplicity of infection
BSL3	biosafety level 3
UTMB	University of Texas Medical Branch at Galveston
PFU	plaque-forming unit
i.n.	intranasal
DPI	days post-infection
Ct	Threshold cycle
DsiRNA	Dicer-substrate short interfering RNA
TBS-T	Tris-buffered saline with 0.1% Tween-20
CMV	cytomegalovirus
HIV-1	human immunodeficiency virus type 1
PRNT	plaque-reduction neutralization test
D130A	aspartic acid residue 130 mutated to alanine
HPI	hours post-infection
SAM	*S*-adenosyl-L-methionine
RLU	relative light unit
DZNep	3-deazaneplanocin A
SAR	structure-activity relationship
LAV	live-attenuated vaccine

Chapter 1 Introduction – An Overview of Viral Dependence on 2'-*O* Methylation

Since its emergence late in 2019, severe acute respiratory syndrome coronavirus 2 (SARS-CoV-2) has caused major damage to the global populace through mortality (*2*), morbidity (*3*), and social and economic disruption (*4*). While the pandemic may be seen as shifting to endemicity, the continued threat of epidemic waves remains due to waning immunity and/or the emergence of new SARS-CoV-2 variants of concern (*5*). Moreover, future outbreaks caused by CoVs seem possible considering previous epidemics this century caused by SARS-CoV and Middle East respiratory syndrome (MERS)-CoV (*6*). Therefore, there is a need to expand our understanding of SARS-CoV-2 and identify additional avenues for treatment.

CoV Emergence in the 21st Century

Prior to the 21st century, CoVs were considered pathogens of minor concern to human health. The CoVs known at the time included two viruses, 229E and OC43, that caused cold-like symptoms and were infrequently associated with more severe respiratory disease (*7*). On the other hand, CoVs were recognized as a possible threat to the livestock and poultry industries, as a few CoVs were known either to cause mortality in piglets or decreased egg production in chickens (*8*).

The current perception of CoVs is now much different. In 2019, SARS-CoV-2, the causative agent of COVID-19, emerged in Wuhan, China under conditions that still remain unclear (*9*), although it was quickly realized that SARS-CoV-2 bore strong resemblance to circulating viruses of the *Sarbecovirus* subgenus, or SARS-related CoVs, found in bats (*10*), and to the original SARS-CoV which emerged in 2002 (*11*), hence the name adopted for this novel CoV. Bats were identified as an animal reservoir for SARS-related CoVs

three years after SARS-CoV emerged (*12*), and eight years after that observation, it was discovered that a SARS-related bat CoV, WIV1, was able to utilize the same human cellular receptor, angiotensin converting enzyme 2 (ACE2), as SARS-CoV (and as would, eventually, SARS-CoV-2) (*10, 13*). Another SARS-related bat CoV, SHC014, was found capable of replicating in human cells and in mouse models (*14*). Thus, even before SARS-CoV-2 emerged, there was an understanding that SARS-related CoVs circulating in the wild harbored a potential for future emergence.

Although the bat reservoir was unknown at the time, the SARS epidemic was linked to intermediate mammalian hosts, namely Himalayan palm civets and raccoon dogs, sold at wildlife markets in Guangdong, China (*15*). Early cases were linked to so-called "super-spreading" events, including one consequential event involving international travelers staying at the same Hong Kong hotel (*16*), and while SARS-CoV spread to many countries globally, it was contained with relatively few cases (~8000) and fatalities (~800) (*17*) compared to the ongoing SARS-CoV-2 pandemic, with cases in the hundreds of millions and fatalities in the millions (*18*). The difference in case numbers and fatalities between SARS-CoV and SARS-CoV-2 may be due, in part, to differences in how the two viruses spread, with asymptomatic transmission uncommon with SARS-CoV (*19*) but a hallmark of SARS-CoV-2 transmission (*20*). The two viruses harbor differences in sensitivity to type I interferon (IFN-I) (*21*), a major component of host innate immunity, which may be mediated by differences in function of so-called "accessory" open reading frames (ORFs) near the 3' end of the genome (*22*). SARS-CoV and SARS-CoV-2 also appear to cause different disease severity given the difference in mortality rates (~10% for SARS-CoV versus ~1% for SARS-CoV-2), but because of the relatively limited clinical data available for SARS, compared to COVID-19, comprehensive comparisons are difficult (*23*).

While more distant, phylogenetically, from the SARS-related CoVs, MERS-CoV is also capable of causing severe respiratory distress (*23*), and, while less cases of MERS-CoV than either SARS-CoV or SARS-CoV-2 have been reported since the emergence of

MERS-CoV in 2012, as of April 2022, new cases of MERS-CoV were still being reported in areas of the Middle East (*24*). The case fatality rate for MERS-CoV is ~35%, more than three times that of SARS-CoV, but MERS-CoV also utilizes a different receptor, dipeptidyl peptidase 4 (DPP4), than do the SARS-related CoVs, perhaps helping to explain why it does not spread as readily (*23*). Similar to SARS-related CoVs, MERS-CoV infection is most severe in the elderly, immunocompromised individuals, and those with chronic conditions (*23, 25*). Dromedary camels can transmit MERS-CoV to humans (*26*), and seropositivity of MERS-CoV in archived camel sera dates back to 1992 (*27*). However, as with SARS-related CoVs, bats appear to be the natural reservoir for MERS-CoV (*28*). Highlighting the ability of emergent CoVs to spread globally, a notable outbreak of MERS-CoV outside of the Arabian Peninsula occurred in 2015, when an infected individual traveling from Saudi Arabia to South Korea initiated an outbreak of MERS-CoV in the latter, involving 186 cases and 38 fatalities, largely due to nosocomial transmission (*29*). In summary, three highly pathogenic CoVs have emerged since the start of the 21st century. The presence of circulating CoVs in natural reservoirs, such as bats, underscores a persistent threat of future CoV emergence.

CoV Replication and the Nonstructural Proteins

CoVs express an array of viral effectors that subvert host immunity to allow for successful replication (*30, 31*). Studies surveying the roles of proteins expressed by SARS-CoV-2 in replication and immune evasion have often relied on ectopic expression of these proteins in immortalized cell lines that, while informative, often cannot fully capture the contributions of viral proteins during viral replication (*32-36*). On the other hand, there have also been studies examining SARS-CoV-2-encoded effector function with live virus generated from reverse genetics systems (*37-41*). Typically, these studies engineer mutations at specific regions of the SARS-CoV-2 genome and observe the effects on replication and virulence (*42-46*). While studies with nonstructural protein 16 (NSP16) of

other CoVs have been conducted (*47-50*), possible variation in importance across the CoV family indicate a need to functionally test SARS-CoV-2 NSP16 in viral replication and pathogenesis studies.

To infect a new cell, CoVs bind a protein at the cell surface (such as ACE2 or DPP4), dependent on the particular CoV, and either fuse the viral membrane with the plasma membrane to release viral contents into the cell, or, alternatively, are trafficked into the cell via the endocytic pathway, and fuse with an endosomal membrane (*51*). Proteolytic processing of the spike protein, mediated by host proteases, activates the membrane-membrane fusion mechanism of the spike protein, and appears dependent on which route of entry CoVs take (*52*). As they are positive-sense viruses, CoVs initiate translation of the viral genome upon its release into the cytoplasm (*51*). Importantly, a large ORF at the 5' end of the genome, ORF1ab, encodes the complete replication-transcription complex (RTC) which replicates, transcribes, and post-transcriptionally modifies CoV RNA (*53*). The RTC comprises the nonstructural proteins (NSPs), so named because, while essential to CoV replication, do not constitute a structural component of the virion itself. The RTC localizes to cytoplasmic ER-derived double membrane vesicles (DMVs), which serve as virus replication factories, while also likely shielding viral RNA from host pattern recognition receptors (PRRs) that detect viral RNA (*51*). There is experimental evidence to suggest that SARS-CoV-2, like other CoVs, replicates in DMVs (*54, 55*).

The nature of the CoV RTC differs from that of related viruses in the order *Nidovirales*, named after the 3' co-terminal, or nested, set of sub-genomic RNA species that are generated during transcription of the viral genome (*56*). Notably, CoVs possess NSP functions that are lacking in smaller nidoviruses, such as arteriviruses, which are significant veterinary pathogens (*57*). These NSP functions include RNA exonuclease function, important for proofreading during replication, which could perhaps explain the larger size of CoV genomes compared to those of arteriviruses (*58*), as well as RNA capping functions, both guanine-N7 methyltransferase (MTase) function as well as 2'-*O*

MTase function (encoded by CoV NSP16), the importance of which is described below (*59*).

CoV NSP16 and Viral RNA Capping

As a nonstructural protein, CoV NSP16 is translated only upon release of the viral genome into the cytoplasm (*51*). NSP16 is translated as part of the largest ORF, ORF1ab, and likely remains associated with other NSPs encoded by ORF1ab after proteolytic cleavage, to form the RTC (*53*).

CoV NSP16 is a ribonucleoside 2'-*O* MTase, catalyzing the transfer of a methyl group to the viral RNA cap structure (*60, 61*). This modification to the viral RNA cap is thought to prevent recognition by the host PRR melanoma differentiation-associated protein 5 (MDA5) and effectors in the interferon-induced protein with tetratricopeptide repeats (IFIT) family (*49, 50*). In experiments with purified proteins, it has been shown that SARS-CoV-2 NSP16 prefers, as substrate, RNA methylated at the N7 position of the guanosine cap (*61*), suggesting that SARS-CoV-2 RNA capping proceeds with guanosine transfer, N7 methylation of the guanosine cap, and finally 2'-*O* methylation of the first transcribed nucleotide by NSP16. Such an order of SARS-CoV-2 viral RNA capping would be consistent with the order postulated for SARS-CoV (*62*). Moreover, by homology with SARS-CoV, N7 methylation of the guanosine is mediated by NSP14 (*62*). Recently, it was shown that the NiRAN (nidovirus RNA-dependent RNA polymerase-associated nucleotidyltransferase) domain of NSP12 has guanylyltransferase activity, and therefore, likely transfers the guanosine cap to nascently synthesized CoV RNA (*63, 64*). Recently, it was suggested that NSP9 may serve as an intermediate substrate for viral RNA attachment immediately before guanosine cap transfer (*64*) (**Figure 1.1**).

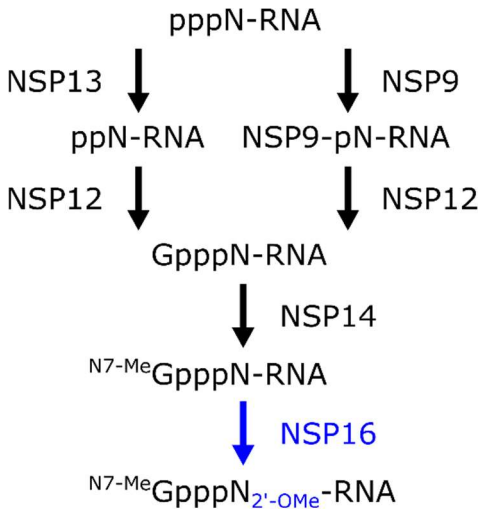

Figure 1.1: RNA Capping Model in CoVs

Newly synthesized viral RNA contains a 5' triphosphate, which may be cleaved by NSP13 (*65*) followed by NSP12-mediated guanosine cap transfer (*63*). Alternatively, NSP9 may form an intermediate with the viral RNA itself prior to guanosine cap transfer (*64*). Regardless, NSP14 methylates the N7 of the guanine base of the cap (*66*). Finally, NSP16 methylates the 2'-*O* of the ribose of the first transcribed nucleotide (*67*).

2'-*O* Methylation in CoVs

Reliance on 2'-*O* methylation has been observed in a broad range of virus families that either encode their own 2'-*O* MTases (*68*), rely on a host 2'-*O* MTase (*69*), or simply "snatch" host mRNA caps to incorporate into their own viral RNA (*70*). Disrupting the ability of these viruses to mimic host RNA cap structure results in a range of attenuation phenotypes (*47, 49, 69, 71*).

In CoVs, the importance of 2'-*O* methylation is well established, including in mouse hepatitis virus (MHV) (*49*) as well as in human CoV 229E (*50*), SARS-CoV (*47*) and MERS-CoV (*48*). These studies utilized mutants of the CoV NSP16 MTase in a conserved lysine-aspartic acid-lysine-glutamate (KDKE) catalytic tetrad necessary for NSP16 MTase function (*50, 72*). The results were striking—ablating the function of even a single amino acid in the catalytic tetrad resulted in highly attenuated CoVs that caused less severe disease in mouse models of CoV infection (*47, 48*). The majority of these studies focused on ablating the aspartic acid (D) of the catalytic tetrad of NSP16. Mutating this one aspartic acid residue alone to an alanine residue was sufficient for the attenuated phenotypes observed. One study also examined mutating either of the two lysines (K) of the catalytic tetrad of SARS-CoV NSP16, which also resulted in CoV mutants that were attenuated, further demonstrating the essential nature of the residues constituting the catalytic tetrad (*47*).

The Innate Antiviral Response to CoV Infection

The first line of defense for an infected host cell against any intracellular pathogen comprises broadly reactive yet finely tunable innate immune signaling pathways, involving PRRs, intermediate immune modulators, transcription factors, and downstream effectors. The PRRs recognize pathogen-associated molecular patterns (PAMPs) such as double-stranded (ds) RNA which is formed during replication of certain RNA viruses (*73*),

cytosolic DNA from invading DNA viruses (*74*), or bacterial components such as lipopolysaccharide (LPS), peptidoglycan, flagellin, or others (*73*).

For RNA viruses, including CoVs, two major classes of PRRs are the Toll-like receptors (TLRs) as well as the retinoic acid-inducible gene I (RIG-I)-like receptors (RLRs), RIG-I and MDA5 (*75*). The membrane-bound TLRs, such as TLR3, TLR7, and TLR8, can detect either dsRNA or structured single-stranded (ss) RNA, associated with certain viruses, as viruses enter the endocytic pathway, whereas the RLRs are present in the cytosol. The RLRs have helicase activity and are activated upon binding dsRNA (*76*). Both the TLRs and RLRs signal through intermediate signaling complexes, which phosphorylate transcription factors such as interferon regulatory factor (IRF)-3 and IRF-7 or release nuclear factor κB (NF-κB) (*77*). These then traffic to the nucleus to prime transcription of type I and/or III interferons (via IRFs and NF-κB), cytokines (via NF-κB), or even a subset of so-called interferon-stimulated genes (ISGs, via IRF-3) (*77-79*). Type I and type III interferons, which share many similarities in how they are induced and the genes they stimulate, differ in the contexts in which they are expressed and the receptors they utilize (*79, 80*). In either case, both type I and type III interferons signal in an autocrine and paracrine manner to activate an antiviral program of hundreds of ISGs (*79*).

Viruses, in aggregate, employ a panoply of tactics to mitigate these innate immune pathways. Numerous examples exist of viruses from diverse virus families encoding factors that bind and suppress the activity of specific components of innate immune signaling, such as those of the IFN-I induction and signaling pathways, where essentially every step of the pathway is inhibited by a known viral protein (*81*).

CoVs are no exception to this rule, encoding many IFN-I antagonists: the papain-like protease (PLP) domain of SARS-CoV NSP3 deubiquitinates and thus antagonizes ubiquitinated components of IFN-I signaling (*82*), MERS-CoV ORF4b interferes with RNase L activation by enzymatically degrading its stimulatory signal (*83*), and several other CoV accessory ORFs as well as CoV nucleocapsid and membrane proteins

antagonize various aspects of IFN-I signaling (*31*). In addition to overt antagonism, CoVs also employ more subtle means to evade detection by host PRRs. In particular, the RNA capping functions encoded by CoVs allow them to evade detection from one important class of ISGs known as the IFIT family.

The IFIT Family

Studies of CoV MTase mutants have underscored the importance of IFIT family members, especially IFIT1, in mediating attenuation of NSP16-deficient CoVs (*47, 48, 50*). IFIT family members are highly expressed during type I interferon (IFN-I) stimulation, and are also inducible by IRF-3; therefore, they are an important component of the early antiviral response (*84*). They have different affinities for RNA cap structures (*85*), which can be modulated by their interactions with each other (*84, 86*), albeit in a species-dependent manner (*84*). Human IFIT1 is sensitive to cap0 structure, *i.e.* an RNA cap lacking 2'-*O* methylation, and can bind itself, IFIT2, IFIT3, or a heterodimer of IFIT2 and IFIT3 (*84*).

Because IFIT1 binds cap0 RNA, it competes with eukaryotic initiation factor (eIF) 4F for binding of RNA cap structures, impeding 48S ribosomal complex formation and thereby inhibiting translation of cap0 RNA (*85*). IFIT1 was also shown to interact with eIF3 via a yeast two-hybrid screen, and exogenous expression of IFIT1 suppressed translation of a reporter protein in a manner dependent on this interaction (*87*). These findings suggest a model of IFIT1 inhibition of cap0 RNA whereby IFIT1, which associates with eIF3, out-competes neighboring eIF4F for binding to cap0 RNA, thus restricting translation of cap0 RNA. In addition to its sensitivity to viral cap0 RNA, IFIT1 can also target host cap0 RNAs (*88*).

Beyond their role in recognizing RNA cap structures, IFIT proteins also have roles in apoptosis, proliferation, and IFN-I induction itself. Exogenous IFIT2 expression induced apoptosis by activating pro-apoptotic, mitochondrion-associated Bak and Bax

proteins (*89*). Conversely, exogenous IFIT3 expression reduced the pro-apoptotic effects of exogenous IFIT2 via binding with IFIT2 (*89*). IFIT3 was separately shown to have antiproliferative effects, by interacting with or upregulating proteins involved with the cell-cycle such as Jun activation domain-binding protein 1 (JAB1) and c-myc (*90*). IFIT1 was shown to bind stimulator of interferon genes (STING) to modulate the interactions of STING with other components of the IFN-I induction pathway (*91*). IFIT3 immunoprecipitated with both MAVS and TANK binding kinase 1 (TBK1) and was necessary for robust IFNβ induction (*92*).

Models of CoV NSP16 MTase Mutant Attenuation

In addition to sensitizing viral RNA to recognition by IFIT family members, presumably due to increased cap0-modified viral RNA, mutation of CoV NSP16 2'-*O* MTase also resulted in higher IFN-I induction upon infection compared to wild-type virus, particularly in bone marrow-derived macrophages (BMDM) (*50*). This phenotype appeared to be due to increased recognition by MDA5, based on a few observations: First, data showed increased IFNβ released into the culture medium of 2'-*O* MTase mutant-infected, compared to WT-infected, BMDMs, suggesting increased induction of IFN-I. Second, this finding was consistent with other data showing increased IRF-3 nuclear localization in 2'-*O* MTase mutant-infected versus WT-infected BMDMs. Third, infection in MDA5$^{-/-}$ BMDMs both restored replication of the 2'-*O* MTase mutant and also abrogated nuclear localization of IRF-3, making nuclear localization levels of IRF-3 equivalent for both WT- and 2'-*O* MTase-mutant-infected BMDMs. However, to date, there has not been a mechanism determined for increased recognition of the viral RNA of 2'-*O* MTase mutants by MDA5, nor was MDA5 detected in a screen of host proteins that bind different RNA cap structures (*93*), although recognition of viral RNA caps sporting non-host signatures by PRRs has precedent: RIG-I, another host PRR, is able to recognize the 5' triphosphate on RNA, an intermediate structure of viral replication (*94*), and may

also recognize cap0 RNA (*95, 96*). An alternate explanation to account for the data in (*50*) is that WT virus, which replicates better than the 2'-*O* MTase mutant, is able to express a higher amount of IFN-I suppressing viral proteins, which would account for the lower IRF-3 nuclearization and lower secreted IFNβ observed (**Figure 1.2**).

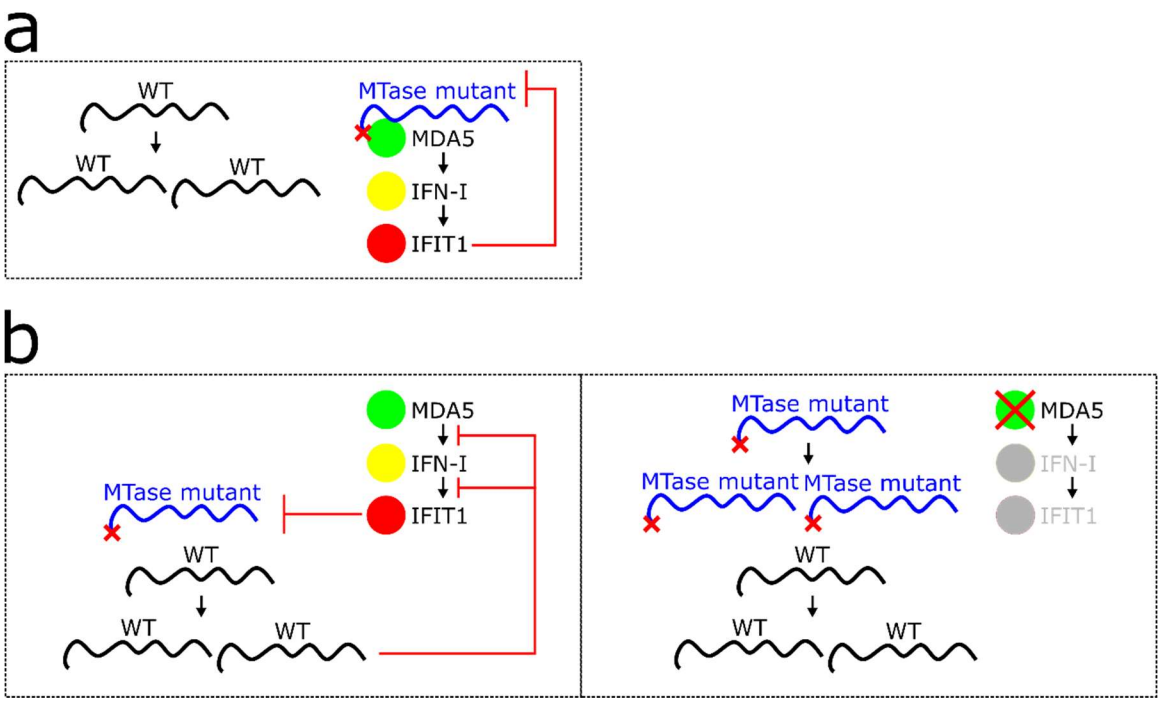

Figure 1.2: Alternative Models of CoV NSP16 MTase mutant attenuation.

(a) Model suggested by (*50*). A lack of 2'-*O* methylation (red "X") on the RNA cap of CoV NSP16 MTase mutant is sensed by MDA5, which in turn induces IFN-I production, resulting in expression of ISGs—importantly, IFIT1—which finally restricts viral RNA lacking cap 2'-*O* methylation, completing a negative feedback loop. In contrast, WT CoV replication proceeds relatively unaffected as it possesses cap 2'-*O* methylation. Other features of this model consistent with data from (*50*) are that the CoV NSP16 MTase mutant, compared to WT, induces higher IRF-3 nuclear localization in an MDA5-dependent manner, induces more IFN-I production, replicates to lower titer, and replicates to similar titer in murine IFIT1$^{-/-}$ BMDMs. (b) An alternative model we present here for the data presented in (*50*). Because WT CoV evades the action of IFIT1 and is therefore able to replicate better than CoV NSP16 MTase mutant, and, further, because it encodes many factors which suppress both IFN-I induction and downstream IFN-I signaling (*33*), it may more effectively suppress IFN-I induction as a direct result of better replication and higher production of antagonists of the IFN-I pathway (left panel). On the other hand, in

the context of MDA5$^{-/-}$ cells, IRF-3 nuclear localization induced by the CoV NSP16 MTase mutant is reduced (*50*), likely resulting in less IFN-I production and downstream ISG (IFIT1) production. This may allow the CoV NSP16 MTase mutant to replicate to similar levels as WT (right panel), as observed (*50*). Of note, MDA5 is known to be a key sensor, and perhaps the primary sensor, of SARS-CoV-2 (*97-99*), and therefore knockout of MDA5 could be expected to significantly affect sensing of the CoV NSP16 MTase mutant and consequent downstream IFN-I signaling.

2'-*O* Methylation in Other Virus Families

Similar to CoVs, flaviviruses, another positive-sense, non-segmented virus family, encode their own 2'-*O* MTases. Interestingly, and distinct from CoVs, flavivirus 2'-*O* MTase activity and guanine-N7 MTase activity are catalyzed by the same domain of a multifunctional protein, nonstructural protein 5 (NS5) (*100*). NS5 is also a guanylyltransferase that catalyzes the guanosine cap transfer (*101*). Together with NS3, which has triphosphatase activity, flaviviruses appear to possess all the functionality for complete capping of flavivirus RNA (*100*). NS5 catalyzes both guanine-N7 methylation on the guanosine cap and 2'-*O* methylation on the adjacent first-transcribed nucleoside (*100*). Similar to CoVs and other virus families encoding ribonucleoside MTases (*102*), the NS5 MTase contains the conserved KDKE catalytic tetrad (*103*). In a cell-free system, NS5 from West Nile virus (WNV) (*104*) or dengue virus (*105*) was dependent on the aspartic acid residue for both guanine-N7 and 2'-*O* MTase activity. Moreover, 2'-*O* MTase activity was also dependent on the other three catalytic residues, whereas guanine-N7 MTase activity was detectable even with mutation of these other three catalytic residues. Similar to CoVs, studies with flavivirus 2'-*O* MTase mutants showed increased sensitivity of those viral mutants to IFN-I and in particular IFIT family members, and which were also attenuated *in vivo* (*49, 86, 106*).

Beyond non-segmented, positive-sense viruses, MTase activity is also encoded by non-segmented, negative-sense viruses including rhabdoviruses (*107*), paramyxoviruses (*108*), and filoviruses (*109*). Beyond single-stranded RNA viruses, MTase activity is also encoded by reoviruses (*110*) and poxviruses (*111*). In all virus families that encode MTase activity, MTase activity appears to be exclusive to 2'-*O* methylation or to guanine-N7 methylation, but not both, as with flaviviruses. Thus, 2'-*O* and N7 methylation are typically encoded by separate proteins. Interestingly, reoviruses encode a 2'-*O* MTase and guanine-N7 MTase on different domains of the same protein (*112*). In all cases, viral

MTases belong to the Rossmann Fold MTase structure superfamily, although they share little sequence identity (*102*).

Viruses need not encode their own MTase to bring about 2'-*O* methylation on their synthesized RNA. For example, HIV-1 RNA associates with host FTSJ3, a cap 2'-*O* MTase also capable of internal RNA 2'-*O* methylation (*69*). HIV-1 from cells depleted of FTSJ3 displayed less internal 2'-*O* methylation on viral RNA (cap 2'-*O* methylation was not surveyed), induced higher IFN-I signaling in an MDA5-dependent manner, and was attenuated *in vitro*. Overall, whether they encode their own MTase functions or not, it appears that many viruses across diverse phylogenies depend on RNA capping of viral RNA for successful replication.

Summary

Evading detection of viral RNA by host sensors is a hallmark of viral replication, and cap 2'-*O* methylation is an important process relied on by many virus families. For CoVs, cap 2'-*O* methylation is mediated by NSP16. In this work, we confirmed the importance of SARS-CoV-2 NSP16 to viral infection and pathogenesis. Building from previous studies of CoV 2'-*O* MTases, we disrupted, via mutagenesis, the KDKE catalytic tetrad necessary for NSP16 MTase function (*50, 72*). We found our NSP16 MTase mutant (dNSP16) was attenuated *in vitro* in the context of IFN-I activity. Additionally, we observed reduced disease and viral loads for dNSP16 in a hamster model of infection. Importantly, we showed that the ISGs IFIT1 and IFIT3 mediate dNSP16 attenuation. Finally, targeting NSP16 activity with the MTase inhibitor sinefungin increased the sensitivity of wild-type (WT) SARS-CoV-2 to IFN-I treatment. Together, these findings demonstrate a key role for NSP16 in SARS-CoV-2 immune evasion and potentially identify CoV 2'-*O* MTase function as a target for novel therapeutic approaches (*113*).

Chapter 2 Materials and Methods

Cell Lines

Vero E6 cells (ATCC #CRL-1586) were cultured in high-glucose Dulbecco's Modified Eagle Medium (DMEM, Gibco #11965–092) supplemented with 5% heat-inactivated fetal bovine serum (FBS, Cytiva #SH30071.03) and 1X Antibiotic-Antimycotic (Gibco #15240-062). VeroE6/TMPRSS2 (JCRB #1819) were cultured in low-glucose, pyruvate-containing DMEM (Gibco #11885-084) supplemented with 5% FBS and 1 mg/mL geneticin (Gibco #10131-035). Calu-3 2B4 (BEI Resources # NR-55340) were cultivated in high-glucose DMEM supplemented with 10% FBS, 1X Antibiotic-Antimycotic, and 1 mM sodium pyruvate (Sigma-Aldrich #S8636). Baby hamster kidney (BHK) cells were cultured in MEM α with GlutaMAX (Gibco # 32561-037) supplemented with 5% FBS and 1X Antibiotic-Antimycotic. For all propagation and experimentation, cells were kept at 37°C and 5% CO_2 in a humidified incubator.

Viruses

We performed PCR-based mutagenesis (New England BioLabs #E0554) according to the manufacturer's protocol to engineer a 2-base pair (bp) mutation in codon 130 of the NSP16 gene encoded on a SARS-CoV-2 infectious clone (ic) reverse genetics system based on the prototype "USA/WA1/2020" strain (NCBI accession no.: MN985325), following our previously published method (*37, 114*) (**Figure 2.1**). The engineered change was made to the second and third bp positions of NSP16 codon 130 (*G<u>AT</u>→G<u>CG</u>*) on pUC57-CoV-2-F5, changing the encoded aspartic acid residue to an alanine. The initially rescued virus constituted a heterogenous population of sequences, therefore the initial stock was serially diluted and plated into wells containing Vero E6 cells to isolate single clones via plaque purification. Individual plaques were carefully scraped with a pipette tip and used to inoculate separate wells containing Vero E6 cells. Upon induction of CPE, culture

supernatants were cleared of cellular debris and part of the liquid fraction processed for viral RNA purification and Sanger sequencing. Well supernatants associated with viral sequences that contained the desired NSP16 mutation were then used to infect TMPRSS2-expressing Vero E6 cells for an additional round of virus replication to generate higher viral titers; TMPRSS2-expressing cells were chosen to reduce the chance of mutation of the spike protein around the furin cleavage site (*115*). The supernatants from these cells were similarly processed as described above for confirmation of viral sequence via Sanger sequencing. Upon sequence verification, a supernatant-stock of icSARS-CoV-2 with the engineered NSP16 mutation ("dNSP16") was selected for use in subsequent experiments. With the exception of the plaque purification step, wild-type icSARS-CoV-2 ("WT") was produced in the same way as dNSP16.

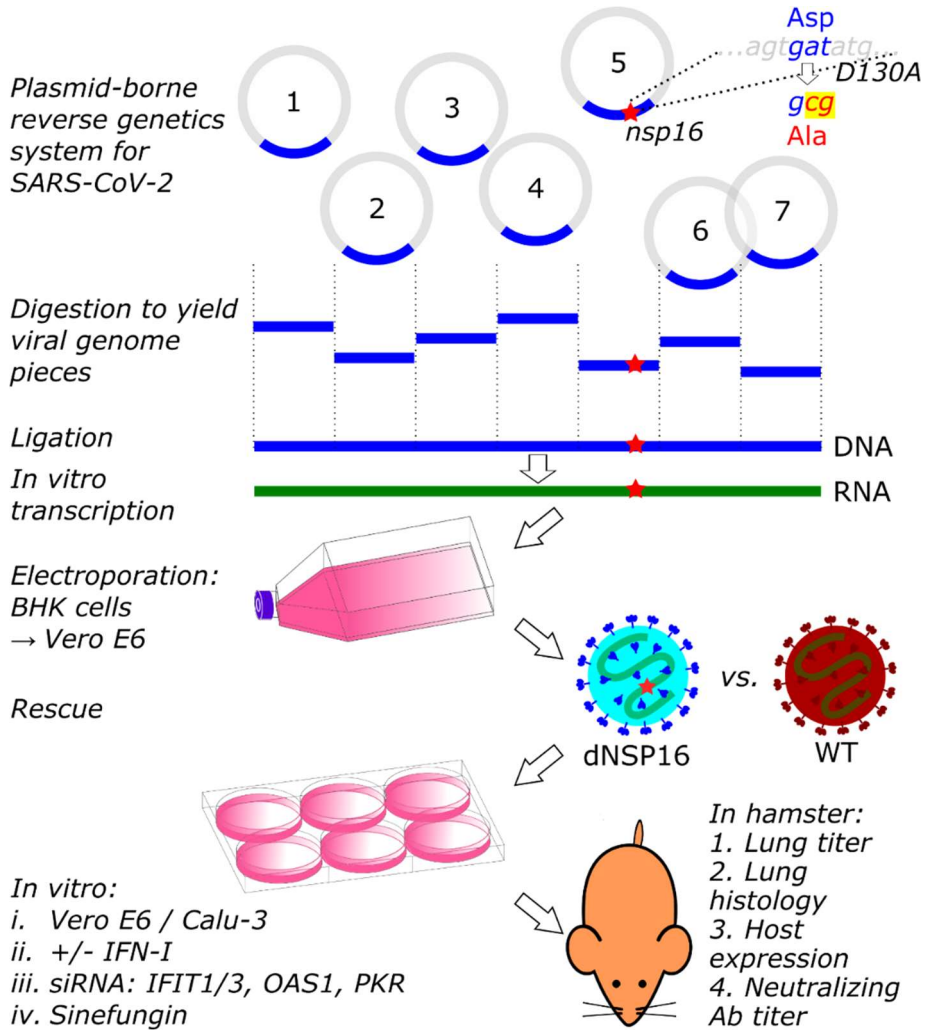

Figure 2.1: General overview of construction of NSP16-mutant SARS-CoV-2 ("dNSP16").

For complete details regarding the reverse genetics system used for this work, please see (*114*). Briefly, a 2 base-pair change (*GAT*→*GCG*) was made to codon 130 of NSP16, changing the encoded aspartic acid to alanine. The mutant fragment (or wild-type fragment for WT SARS-CoV-2) was excised out of pUC57-CoV-2-F5 and ligated with other plasmid-borne fragments of the reverse genetics system to generate full-length SARS-CoV-2 cDNA, which was transcribed to full-length infectious RNA *in vitro* and then electroporated into BHK cells, which were subsequently seeded on top of Vero E6 cells. Upon induction of cytopathic effect (CPE), supernatants were collected, further

amplified on TMPRSS2-expressing Vero E6 cells, analyzed for sequence integrity, and subsequently used for the experiments described herein.

Viral Replication Kinetics

Cells were seeded in 24-well format. In experiments involving IFN-I pre-treatment, cells were treated 16 – 20 hours prior to infection with Universal Type I IFN (PBL Assay Science #11200-2), diluted in Dulbecco's phosphate-buffered saline, without calcium chloride and magnesium (DPBS, Gibco #14190-144). After infection at a multiplicity of infection (MOI) of 0.01 and incubation for 45 minutes at 37°C with 5% CO_2 and manual tilting every 15 minutes, cells were washed 3X with 500 µL DPBS and then given 500 µL of cell type-specific medium. Supernatants were collected within 1 hour of the indicated time point whereupon 150 µL of culture medium was removed and an equal volume of fresh medium was added back to the sample well. Supernatant samples were subsequently titered via plaque assay. All conditions were performed in triplicate, and all experiments were performed in an approved biosafety level 3 (BSL3) laboratory at the University of Texas Medical Branch at Galveston (UTMB).

Plaque Assay

One day before the assay, 6-well plates were seeded with 3×10^5 Vero E6 cells/well. Under BSL3 conditions, samples of virus-containing supernatant were titrated in a 10-fold dilution series in DPBS, and 200 µL of each dilution of the series was transferred to confluent cells after culture medium was removed. Assay plates were incubated at 37°C with 5% CO_2 for 45 minutes with manual tilting every 15 minutes. Afterwards, an overlay of 1X Modified Eagle Medium (Gibco #11935-046) containing 5% heat-inactivated FetalClone II (Cytiva #SH30066.03), 1X Antibiotic-Antimycotic, and 1% agarose (Lonza #50004) was applied to wells, and the plates were returned to the incubator for two days. Afterwards, a 1X dilution in DPBS of 10X neutral red stain (0.85% w/v NaCl, 0.5% w/v Fisher Scientific #N129-25) was applied to each well, and 2 – 5 hours later, plaque-forming units (PFU) were visualized using a lightbox and manually counted. The limit of detection

was 50 PFU/mL, corresponding to 1 PFU in the well with the lowest dilution factor (1:50 total dilution).

Animal Studies

Four- to five-week-old male Syrian hamsters (*Mesocricetus auratus*), strain HsdHan:AURA, purchased from Envigo were infected intranasally (i.n.) with a 10^4 PFU dose of either dNSP16 or WT in a 100 uL inoculum volume, or DPBS for mock-infected animals. Hamsters were randomly assigned to different treatment groups. Animal weights and clinical signs were recorded daily for up to 7 days post-infection (DPI). Disease scores were as follows: 1 (healthy), 2 (ruffled fur), 3 (hunched posture, orbital tightening, lethargy), 4 (moribund). At 2, 4, and 7 DPI, nasal washes from 5 animals from each experimental group were collected and the animals subsequently sacrificed, with right cranial, right middle, and left lung lobes from each animal collected in either DPBS, RNAlater (Invitrogen #AM7021), or 10% phosphate-buffered formalin (Fisher #SF100) for subsequent analyses of viral titer, gene expression and viral sequence, or histopathology, respectively. For measurement of viral titer, collected lung lobes were homogenized at 6000 rpm for 60 seconds using a Roche MagNA Lyser instrument and then titered via plaque assay. For analysis of gene expression and viral sequence, lung lobes stored in RNAlater were transferred to TRIzol (Invitrogen #15596018) and homogenized 5 times at 6500 rpm for 30 seconds, with cooling on a –20°C-chilled rack for 1 minute between homogenization steps. The homogenates were then processed for RNA purification as described below. For histopathological analysis, lung lobes were incubated with 10% phosphate-buffered formalin for 7 days at 4°C to allow for deactivation and buffer exchange before processing. All animal handling was performed at animal biosafety level 3 (ABSL3) conditions and in accordance with guidelines set by the Institutional Animal Care and Use Committee (IACUC) of the University of Texas Medical Branch.

Histology

For visualization of histopathology, sections of paraffin-embedded formalin-fixed tissue were stained with hematoxylin and eosin on a SAKURA VIP 6 tissue processor at the University of Texas Medical Branch Surgical Pathology Laboratory. For visualization of viral antigen, tissue sections were deparaffinized and stained with a SARS-CoV-2 N-specific rabbit monoclonal antibody (Sino Biological #40143-R001) at a dilution of 1:30,000 followed by an anti-rabbit HRP-linked secondary (Cell Signaling #7074). Signal was developed with ImmPact NovaRED peroxidase kit (Vector Labs # SK-4805).

RNA Purification

RNA from cell supernatants, cell lysates, or homogenized lung tissue was extracted in TRIzol LS (Invitrogen #10296010) for cell supernatants only or TRIzol, followed by purification using Direct-zol RNA Miniprep Plus (Zymo Research #R2072) and reverse transcription using iScript cDNA synthesis kit (Bio-Rad #1708891).

Sanger Sequencing

Phusion High-Fidelity PCR Master Mix with HF Buffer (New England BioLabs #M0530) was used to amplify cDNA around the region of interest. 45 amplification cycles were used; otherwise the manufacturer's protocol was followed. To amplify the region encoding NSP16, forward primer 5'- AACAGATGCGCAAACAGG and reverse primer 5'- TGCAGGGGGTAATTGAGTTC were used. To amplify the region of spike in the vicinity of the furin cleavage site, forward primer 5'- AGGCACAGGTGTTCTTAC and reverse primer 5'-TGAAGGCTTTGAAGTCTGCC were used. Amplicons were verified by gel electrophoresis, purified using QIAquick PCR Purification Kit (QIAGEN #28106), and sent to Genewiz (South Plainfield, NJ) for Sanger sequencing.

Gene Expression via Quantitative PCR (qPCR)

qPCR was performed on cDNA using Luna (New England BioLabs #M3003) according to the manufacturer's instructions. Fluorescent readings were made on a Bio-Rad CFX Connect instrument using Bio-Rad CFX Maestro 1.1 software (version 4.1.2433.1219). Relative gene expression was calculated manually using the ΔΔCt method: For each cDNA sample, the threshold cycle (Ct) of the gene of interest was first normalized against the Ct of the indicated reference gene. Then, the fold change in normalized expression for the gene of interest in each sample was calculated relative to normalized expression of the gene of interest in the control sample. The primers used for amplifying hamster targets are listed in **Table 2.1**. The primers used for amplifying targets in Vero E6 cells are given in **Table 2.2**. All primers were purchased as single-stranded DNA oligomers purified with standard desalting (Integrated DNA Technologies, Coralville, Iowa).

DsiRNA Experiments

Dicer-substrate short interfering RNAs (DsiRNAs) (Integrated DNA Technologies) utilized are given in **Table 2.3**. For a negative control DsiRNA construct, Negative Control DsiRNA (Integrated DNA Technologies #51-01-14-03) was used. For DsiRNA experiments, 1.25 x 10^5 Vero E6 cells/well were reverse transfected in 24-well plate format with 1 – 2 pmol/well DsiRNA as indicated, 2 days prior to infection. 16 – 20 hours prior to infection cells were treated with 100 U of DPBS-diluted Universal Type I IFN (PBL Assay Science #11200-2). Infections proceeded as described in the section "viral replication kinetics" above.

Protein Expression via Western Blot

Cell lysates were harvested with 2X Laemmli SDS-PAGE sample buffer (Bio-Rad #1610737) containing a final concentration of 5% β-mercaptoethanol (Bio-Rad #1610710). Cell lysates were then denatured at 95°C for 10 min. The lysates were then loaded onto a

Mini-PROTEAN TGX gel (Bio-Rad #4561096) and electrophoresed, followed by transfer to a polyvinylidene difluoride membrane (Bio-Rad #1620177). The membrane was then blocked in 5% nonfat dry milk dissolved in Tris-buffered saline with 0.1% Tween-20 (TBS-T) for 1 hour, followed by a short TBS-T wash. Overnight incubation with primary antibody, either rabbit anti-hIFIT1 (Cell Signaling Technology #14769) or rabbit anti-β-actin (Cell Signaling Technology #4970) was then performed. After, the membrane was washed 3 times with TBS-T and incubated with horseradish peroxidase-conjugated secondary antibody (Cell Signaling Technology #7074) for 1 hour. Finally, the membrane was washed 3 times with TBS-T, incubated with Clarity Western ECL Substrate (Bio-Rad #1705060), and imaged with a Bio-Rad ChemiDoc Imaging System running Bio-Rad Image Lab Touch software (version 2.4.0.03).

Overexpression of IFIT Proteins

8.5×10^4 Huh7 cells/well were reverse transfected with 0.8 µg total of pcDNA3-EGFP (a gift from Doug Golenbock, Addgene #13031), pcDNA3.1 3xFlag IFIT1 (*116*) (a gift from Kathleen Collins, Addgene #53554), pcDNA3.1 3xFlag IFIT3 (*116*) (a gift from Kathleen Collins, Addgene #53553), or both pcDNA3.1 3xFlag IFIT1 and pcDNA3.1 3xFlag IFIT3 two days prior to infection. pcDNA3 and pcDNA3.1 have minor differences in restriction sites, but the same cytomegalovirus (CMV) immediate early promoter. Infections proceeded as described in the section "viral replication kinetics" above.

Viability Assay

1.0×10^3 cells/well were seeded in 96-well format. One day later, cells were treated with sinefungin, in parallel to infection experiments with sinefungin. Two days post-sinefungin treatment, cell viability was measured using CellTiter-Glo Luminescent Cell Viability Assay (Promega # G7570). Luminescence was read on a Tecan Infinite 200 PRO running Tecan i-control software (version 2.0.10.0), using an integration time of 1 second.

NSP10 Peptide Design

Two peptides consisting of amino acids 47 – 58 of human immunodeficiency virus type 1 (HIV-1) Tat protein (YGRKKRRQRRR), a three amino acid (GSG) linker, and amino acids 68 – 96 of SARS-CoV-2 NSP10 (amino acids 4321 – 4349 of ORF1a), FGGASCCLYCRCHIDHPNPKGFCDLKGKY, or a randomly scrambled control, GYIGCCKGKHLGLPAFPCRDCKCDHSNYF, were synthesized by GenScript (Piscataway, NJ). Peptides were C-terminus amidated and N-terminus acetylated by the manufacturer.

Plaque-Reduction Neutralization Test

Plaque-reduction neutralization tests (PRNTs) were performed by first incubating serum samples at 56°C for 30 minutes to inactivate complement. Serum samples were then two-fold serially diluted resulting in a final range of dilution factors of 1:20 through 1:640. To each dilution point, WT SARS-CoV-2 virus was added and the serum-virus complexes incubated for 1 hour at 37°C and 5% CO_2 in a humidified incubator, after which 0.2 mL of serum-virus complex (containing 100 PFU WT SARS-CoV-2) was transferred to 6-well plates seeded with Vero E6 cells at 90% confluency, and plaque assays were performed as described in the section "Plaque Assay." $PRNT_{50}$ was defined as the serum dilution factor which resulted in a 50% reduction in the number of plaques, compared to the average of serum-free controls (after outliers were removed). To calculate $PRNT_{50}$, four-parameter logistic curves were fitted to plots of plaque count versus serum dilution using GraphPad Prism, and the $PRNT_{50}$ interpolated from the resulting curves. All PRNTs were performed in technical duplicates on serum samples.

Morpholino Design and Treatment

An octa-guanidine dendrimer-linked antisense morpholino (5'-CTCATATAAGGGCTGGGAAGCAGCT-3'), *i.e.* "Vivo-Morpholino" (GeneTools,

Philomath, OR), was designed to target the 5' untranslated region of *Mesocricetus auratus* (Syrian hamster) interferon-induced protein with tetratricopeptide repeats 1-like (GenBank accession no.: XM_040745240). At both 2- and 1-day prior to infection, four- to five-week-old hamsters were anaesthetized with isoflurane and given 370 ng (36 nmoles) of sterile water-dissolved morpholino or a non-targeting control morpholino (GeneTools #PCO-VivoStandardControl-100) in a 72 µl inoculation volume intranasally.

Statistics

All statistics were performed in GraphPad Prism 9 (version 9.0.2), with details given in figure legends. Two-way ANOVA was performed on $\log_{10}$-transformed viral titers, with Tukey's multiple comparison test ($\alpha = 0.05$) to infer significant differences. For qPCR data, one-way ANOVA was performed on $\log_2$-transformed $\Delta\Delta$Ct values, with Tukey's multiple comparison test ($\alpha = 0.05$) to infer significant differences. For animal weight data, a mixed-effects model (restricted maximum likelihood) was used, with Tukey's multiple comparison test ($\alpha = 0.05$) to infer significant differences. For animal experiments, a group size of $n = 5$ animals per condition per time point was chosen based on previous studies (*45*). For all data at or below the limit of detection, values were set to the limit of detection.

Target	**Forward Primer (5' → 3')**	**Reverse Primer (5' → 3')**
18S	GTAACCCGTTGAACCCCATT	GTAACCCGTTGAACCCCATT
pan-IFIT1	TGCAGAGCTTGAAAGAAGCA	CCTTCCTCACAGTCCACCTC
IFIT3	CCTGGAGTGCTTAAGGCAAG	TGCCTCACCTTGTCCACATA
RNase L	CCAGAGGGTAAAAACGTGGA	TGCACCAAACCTGTGTGTTT
PKR	AAGTGCGTGAAGTAAAGGCG	ATCCATTGCTCCAGAGTCCC
Mx1	CTTCAAGGAGCACCCACACT	CTTGCCCTCTGGTGACTCTC
IFNγ	GGCCATCCAGAGGAGCATAG	TTTCTCCATGCTGCTGTTGAA
IL-1β	GGCTGATGCTCCCATTCG	CACGAGGCATTTCTGTTGTTCA
IL-10	GTTGCCAAACCTTATCAGAAATGA	TTCTGGCCCGTGGTTCTCT

Table 2.1: Primers used for amplifying hamster targets.

Target	**Forward Primer (5' → 3')**	**Reverse Primer (5' → 3')**
β-*actin*	GGCATCCTCACCCTGAAGTA	GGGGTGTTGAAGGTCTCAAA
IFIT1	ACACCTGAAAGGCCAGAATG	GCTTCTTGCAAATGTTCTCC
IFIT3	AGGAAGGGTGGACACAACTG	TGGCCTGTTTCAAAACATCA
OAS1	GATCTCAGAAATACCCCAGCCA	AGCTACCTCGGAAGCACCTT
PKR	ACGCTTTGGGGCTAATTCTT	TTCTCTGGGCTTTTCTTCCA

Table 2.2: Primers used for amplifying targets in Vero E6 cells.

Target	Sequence (5' → 3')
IFIT1	(+) rGrCrUrUrGrArGrCrCrUrCrCrUrUrGrGrGrUrUrCrGrUrCTA
	(–) rUrArGrArCrGrArArCrCrCrArArGrGrArGrGrCrUrCrArArGrCrUrU
IFIT3	(+) rArGrCrUrGrArGrUrCrCrUrGrArUrArArCrCrArArUrArCGT
	(–) rUrArGrUrUrUrArUrGrArCrUrArArUrUrCrCrArArGrArCrCrGrUrC
OAS1	(+) rCrGrGrUrCrUrUrGrGrArArUrUrArGrUrCrArUrArArArCTA
	(–) rUrArGrUrUrUrArUrGrArCrUrArArUrUrCrCrArArGrArCrCrGrUrC
PKR	(+) rGrUrArUrUrGrGrUrArCrArGrGrUrUrCrUrArCrUrArArACA
	(–) rUrGrUrUrUrArGrUrArGrArArCrCrUrGrUrArCrCrArArUrArCrUrA

Table 2.3: Dicer-substrate short interfering RNAs (DsiRNAs) used for gene expression knockdown.

DsiRNAs were used in pairs of positive- (+) and negative- (–) sense oligonucleotides.

Chapter 3 SARS-CoV-2 Uses Nonstructural Protein 16 to Evade Restriction by IFIT1 and IFIT3

dNSP16 Has No Replication Defect

To investigate the contribution of NSP16 to SARS-CoV-2, we constructed dNSP16 using our infectious clone of SARS-CoV-2 as previously described (*37, 114*). Briefly, we generated a 2-base pair substitution, converting aspartic acid to alanine (D130A) in the conserved KDKE motif (**Figure 3.1a, b**). This residue is predicted to be essential to SARS-CoV-2 NSP16 MTase function (*62*). Specifically, prior studies with purified SARS-CoV NSP16 have shown that the D130A mutation completely ablates MTase activity in a cell-free system (*62*). Prior CoV studies have confirmed the importance of this residue to CoV replication and pathogenesis (*47-50, 117*). We also attempted to construct an NSP16 deletion-virus by engineering an in-frame stop codon at the first amino acid position, but this deletion mutant failed to replicate. In IFN-deficient Vero E6 cells, dNSP16 displayed replication kinetics (**Figure 3.1c**) and plaque sizes similar to those of WT (**Figure 3.1d**). Together, these results suggest no significant impact on viral replicative capacity with the loss of NSP16 catalytic activity. Importantly, the D130A mutation was found to be stable in our rescued dNSP16 stock by Sanger sequencing and we confirmed no common spike mutations in the region adjacent to the furin cleavage site that have been previously reported for virus stocks amplified on Vero E6 cells (*44, 115*) (**Figure 3.2**).

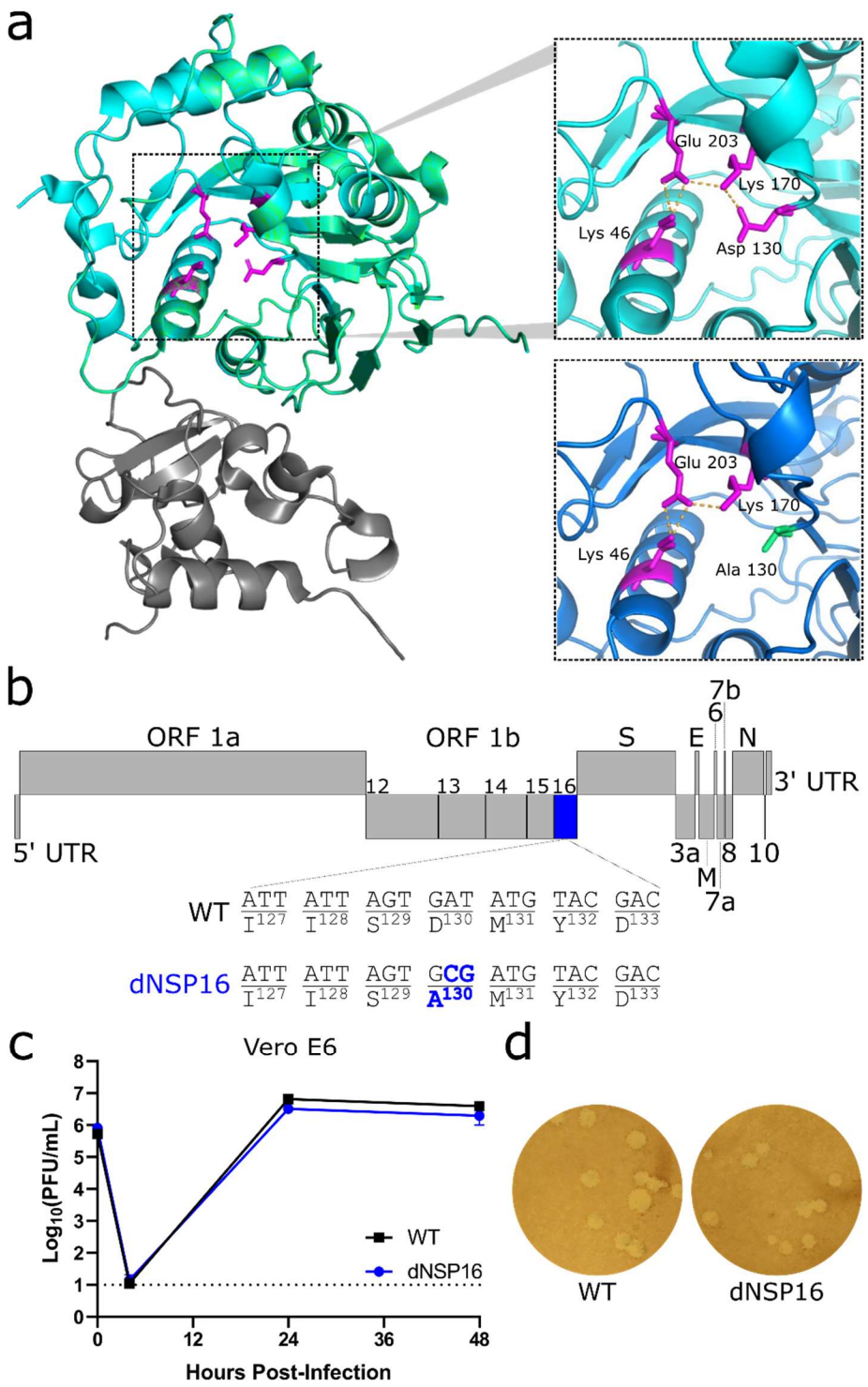

Figure 3.1: dNSP16 has no replication defect.

(a) SARS-CoV-2 NSP16 (green) in complex with scaffold NSP10 (gray). The upper inset shows the KDKE catalytic tetrad (in magenta, with amino acids labeled) with

polar contacts shown by orange dashed lines. The right panel shows mutation of the KDKE motif to KAKE (D130A). The structural modeling demonstrates a loss of a hydrogen bond between K170 and A130. Structures based on Protein Data Bank ID: 6W4H with homology model made using Swiss-Model (*113*). (b) Schematic of the SARS-CoV-2 genome, drawn to scale, with NSP16 highlighted in blue and the engineered two-base change indicated, resulting in coding change D130A. (c) Replication of WT (black) and dNSP16 (blue) in Vero E6 cells, multiplicity of infection = 0.01; $n = 3$. Means are plotted with error bars denoting standard deviation. Dotted line represents limit of detection. PFU = plaque-forming units. (d) Plaque morphology of the WT and dNSP16 viruses on Vero E6 cells.

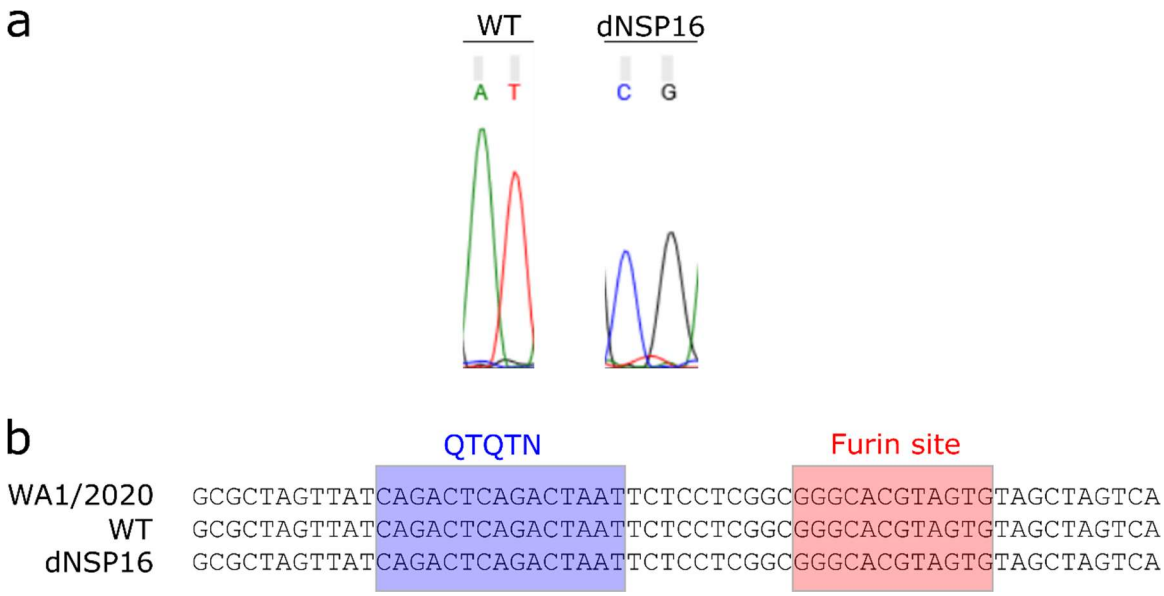

Figure 3.2: D130 mutation is stable in rescued dNSP16, and rescued infectious clone stocks maintain sequence around furin cleavage site.

Viral RNA was extracted from the viral stocks used in the study ("WT" and "dNSP16"). Viral RNA was reverse-transcribed, PCR-amplified around the site of interest, and Sanger sequenced. (a) Shown are the sequencing traces of the 2-base pair site within codon 130 of NSP16 that was mutated from AT to CG to engineer dNSP16. (b) Validated sequence around the furin cleavage site, including the QTQTN motif, for WT and dNSP16, compared to the published sequence for WA1/2020.

dNSP16 is Attenuated in Human Respiratory Cells

While the dNSP16 mutant had no replicative attenuation in Vero E6 cells, phenotypes in these cells are often not representative of relevant cells such as human respiratory cells (*43-45*). Therefore, we next evaluated dNSP16 in Calu-3 2B4 cells, a human lung carcinoma cell line. Compared to WT SARS-CoV-2, we observed significant attenuation of dNSP16 in Calu-3 2B4 cells (**Figure 3.3a**), similar to what has recently been reported for another engineered NSP16 MTase-mutant of SARS-CoV-2 (*118*). At both 24 and 48 hours post-infection (HPI), WT SARS-CoV-2 displayed robust replication whereas a 2.5 $\log_{10}$ decrease in replication was observed for dNSP16 at both time points. These results are consistent with similar findings for both SARS-CoV and MERS-CoV 2'-*O* MTase mutants (*47, 48*). Together, the results confirm the requirement of NSP16 for successful SARS-CoV-2 infection of human respiratory cells.

dNSP16 is More Sensitive to IFN-I Pre-Treatment

A major distinction between Vero E6 and Calu-3 2B4 cells is their capacity to induce an IFN-I response; while Calu-3 2B4 cells are IFN-I competent, Vero E6 cells do not induce IFN-I, but do respond to it when treated exogenously. Therefore, we investigated the effects of IFN-I on the replication of dNSP16 relative to WT. Pre-treating Vero E6 cells with 100 U of IFN-I, we noted a modest, but significant decrease in WT infection compared to untreated cells (**Figure 3.3b**). In contrast, Vero E6 cells pre-treated with IFN-I resulted in 3.0 $\log_{10}$ and 4.2 $\log_{10}$ decreases in dNSP16 titer at 24 and 48 HPI, respectively. We observed a dose-dependent decrease in titer with respect to IFN-I pre-treatment for both dNSP16 and WT; however, the effect on dNSP16 was more pronounced, especially at higher IFN-I concentrations (**Figure 3.3c**). Overall, the results indicate that dNSP16 is more sensitive to IFN-I compared to WT SARS-CoV-2.

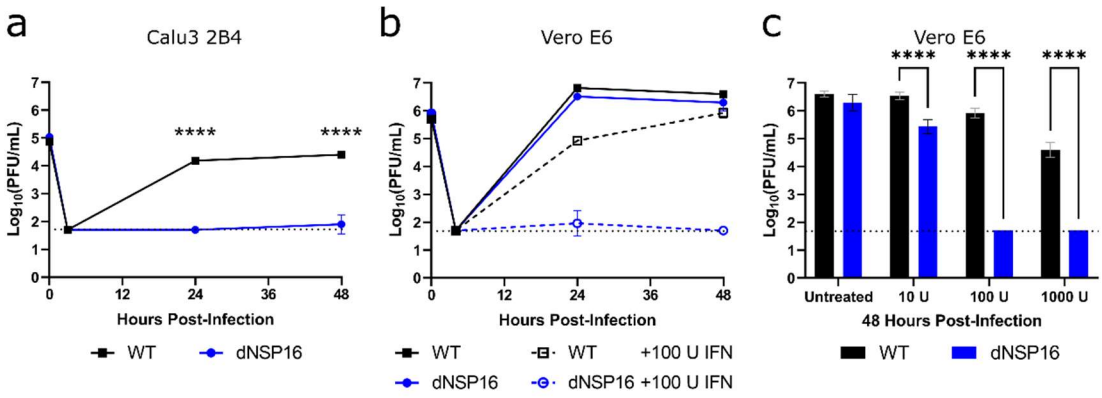

Figure 3.3: dNSP16 is attenuated in human respiratory cells and is more sensitive to type I interferon (IFN-I) pre-treatment.

(a) Replication of WT (black) and dNSP16 (blue) in Calu-3 2B4 cells, MOI = 0.01. ****p<0.001: results of two-way ANOVA with Tukey's multiple comparison test (α = 0.05). (b) Replication of WT (black) and dNSP16 (blue) in Vero E6 cells without IFN-I (solid lines, data as in Fig. 1c), or with 100 U IFN pre-treatment a day prior to infection (dashed lines), multiplicity of infection = 0.01. (c) Comparison of the viral titers at 48 hours post-infection from panel (b), with additional treatment levels of IFN-I indicated. ****p<0.001: results of two-way ANOVA with Tukey's multiple comparison test (α = 0.05). Means are plotted with error bars denoting standard deviation. For all panels, n = 3 for all data points. Dotted lines represent limits of detection. PFU = plaque-forming units.

dNSP16 is Attenuated *In Vivo*

We next asked whether the attenuation of dNSP16 we observed *in vitro* would manifest *in vivo*. We challenged Syrian (golden) hamsters, a model for SARS-CoV-2 infection studies (*119*), intranasally (i.n.) with 10^4 plaque-forming units (PFU) of dNSP16, WT, or a mock-infection control (**Figure 3.4a**). While both dNSP16- and WT-infected hamsters showed weight loss relative to the mock-infected control hamsters, the dNSP16-infected hamsters showed reduced weight loss compared to WT-infected hamsters (**Figure 3.4b**). Moreover, the dNSP16-infected hamsters did not show signs of disease, and only the WT-infected hamsters displayed ruffled fur at 5 and 6 days post-infection (DPI)(**Figure 3.4c**). Lung histopathologic findings were more severe for WT-infected hamsters compared to dNSP16-infected hamsters at both 4 DPI and 7 DPI (**Figure 3.4d**). Both groups developed interstitial pneumonia, bronchiolitis, peribronchiolitis, perivasculitis, and perivascular edema. WT-infected hamsters experienced a greater degree of subendothelial edema and hemorrhage. Together, these results indicate that dNSP16 results in reduced disease in the hamster model of SARS-CoV-2 infection.

To explore why disease phenotype differed in dNSP16-infected hamsters, we first evaluated changes in the host immune response following infection with dNSP16. Examining RNA from hamster lungs collected at 2 DPI, we observed that both WT- and dNSP16-infected samples had increased expression of ISGs (IFIT1, IFIT3, RNase L, PKR, and Mx1) as well as other immune genes (IFNγ, IL-1β, IL-10) **Figure 3.5**) relative to mock. However, no differences in gene expression were observed between WT- and dNSP16-infected hamsters; these data correspond to previous findings with a SARS-CoV 2'-*O* MTase mutant (*47*). Our results suggest the loss of NSP16 activity may not drive increased immune gene expression but rather sensitize dNSP16 to immune gene activity otherwise ineffective against WT SARS-CoV-2.

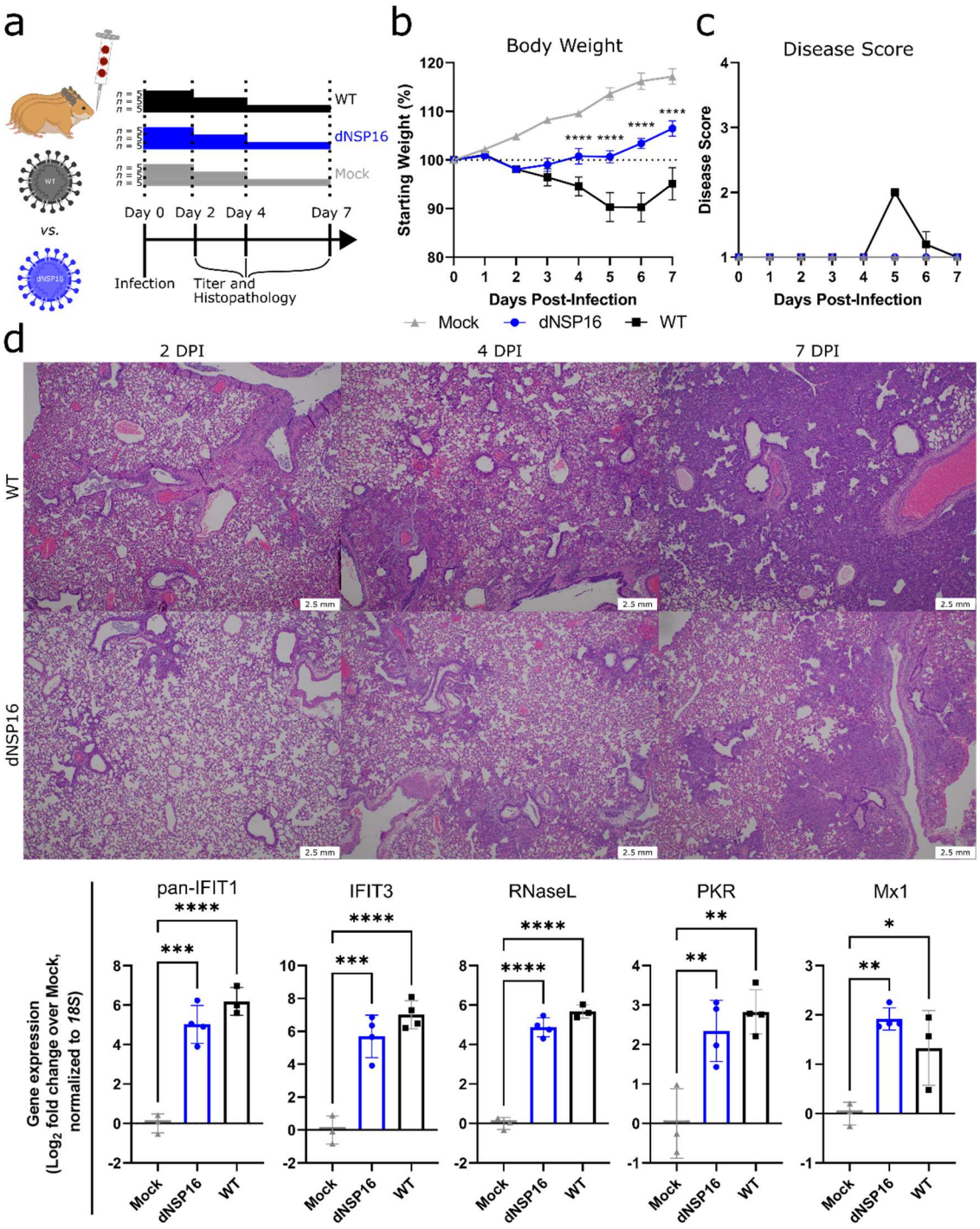

Figure 3.4: dNSP16 is attenuated *in vivo*.

(a) Overview of experimental plan for hamster infections. 100 µL inoculum of PBS (mock) or either dNSP16 (10^4 plaque-forming units) or WT (10^4 plaque-forming units) was given intranasally to 4- to 5-week-old Syrian hamsters. At 2, 4, and 7 days post-infection

(DPI), 5 animals from each infection group were sacrificed for organ collection. (b) Percent starting weights and (c) disease scores for mock-, dNSP16-, or WT-infected hamsters. ****p<0.001: results of a mixed-effects model (restricted maximum likelihood) with Tukey's multiple comparison test (α = 0.05) performed between WT- and dNSP16-infected hamsters at the indicated DPI. Means are plotted with error bars denoting standard error of the mean. (d) Hematoxylin and eosin staining of representative 5 µm-thick sections taken from left lung lobes. (e) Fold change ($\log_2$) of expression of the indicated immune genes from right middle lung lobes isolated from hamsters infected with the indicated virus (or mock), 2 DPI. For each panel, fold changes from dNSP16 or WT samples are measured relative to mock samples. Values from individual hamsters are plotted (symbols) as well as means (bars). Error bars denote standard deviation. All samples were normalized to 18S expression, used as a reference. *p<0.05, **p<0.01, ***p<0.005, ****p<0.001: results of one-way ANOVA with Tukey's multiple comparison test (α = 0.05). Adapted from "Hamster (lateral)", by BioRender.com (2022). Retrieved from https://app.biorender.com/biorender-templates.

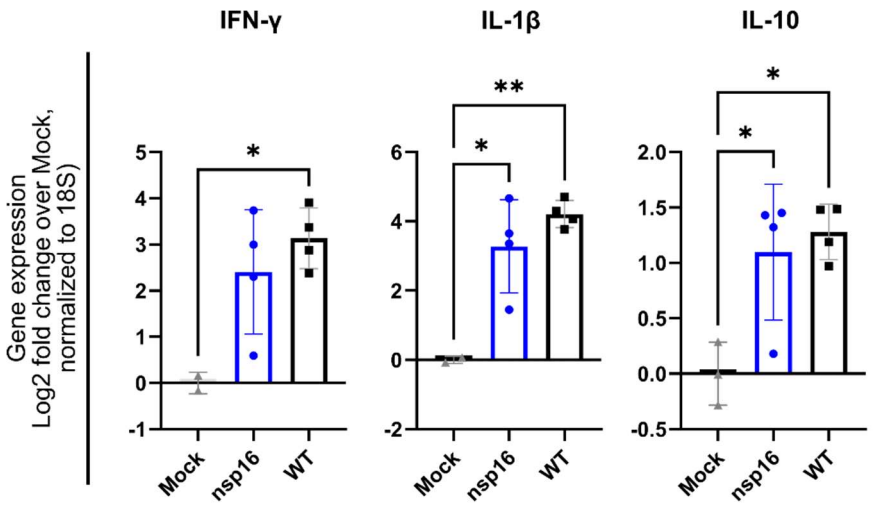

Figure 3.5: dNSP16 does not drive increased immune gene expression relative to WT.

Fold change ($\log_2$) of expression of the indicated immune genes from lung samples isolated from hamsters infected with the indicated virus (or mock), 2 days post-infection. For each panel, fold changes from dNSP16 or WT samples are measured relative to mock samples. Values from individual hamsters are plotted (symbols) as well as means (bars). Error bars denote standard deviation. All samples were normalized to 18S expression, used as a reference. *p<0.05, **p<0.01, *p<0.005, ****p<0.001: results of one-way ANOVA with Tukey's multiple comparison test (α = 0.05).

dNSP16 Replication is Reduced *In Vivo*

We next evaluated viral load in dNSP16-infected versus WT-infected hamsters. Examining replication in the lung, we observed similar viral loads at 2 DPI between dNSP16- and WT-infected hamsters (**Figure 3.6a**); however, by 4 DPI, dNSP16 titer was reduced. This delayed attenuation in the lung corresponds to previous reports for both SARS-CoV and MERS-CoV in mice (*48, 120*). However, nasal wash titers at both 2 and 4 DPI were lower for dNSP16- compared to WT-infected hamsters (**Figure 3.6b**). These nasal wash titer data suggest attenuation of dNSP16 occurs in the upper airway at an earlier time compared to lung and may demonstrate different tissue-mediated immune responses. Notably, while viral titers in the lung were equivalent at 2 DPI, nucleocapsid-specific staining of lung tissue showed more pervasive staining for WT- compared to dNSP16-infected tissues (**Figure 3.6c**). This trend was exacerbated at 4 DPI and corresponded to the difference in titer observed between dNSP16- and WT-infected hamsters (**Figure 3.6a**). Consistent with differences in fitness *in vivo*, targeted Sanger sequencing of viral RNA from the lungs at 4 DPI showed no signs of reversion in the dNSP16-infected hamsters (**Figure 3.7**). Together, these results indicate that dNSP16 causes reduced disease and exhibits decreased viral replication *in vivo* despite inducing an immune response similar to that of WT SARS-CoV-2.

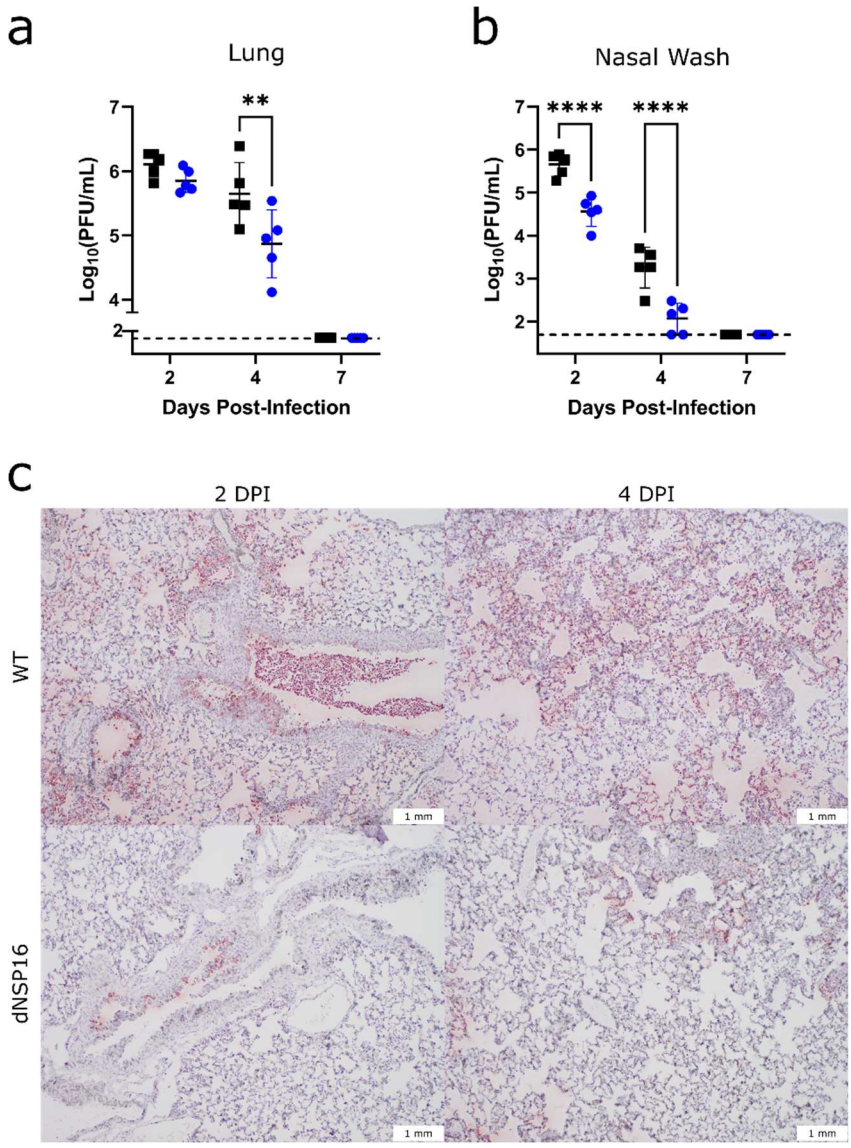

Figure 3.6: dNSP16 replication is reduced *in vivo*.

(a, b) Comparison of viral titers from (a) right cranial lung lobes or (b) nasal washes from WT- (black) or dNSP16-infected (blue) hamsters sacrificed at the indicated day. $^{**}p<0.01$, $^{****}p<0.001$: results of two-way ANOVA with Tukey's multiple comparison test ($\alpha = 0.05$). Values from individual hamsters are plotted (symbols) as well as means (black bars). Error bars denote standard deviation. Dotted lines represent limits of detection. PFU = plaque-forming units. (c) SARS-CoV-2 nucleocapsid staining (brown) of representative 5 µm-thick sections taken from left lung lobes.

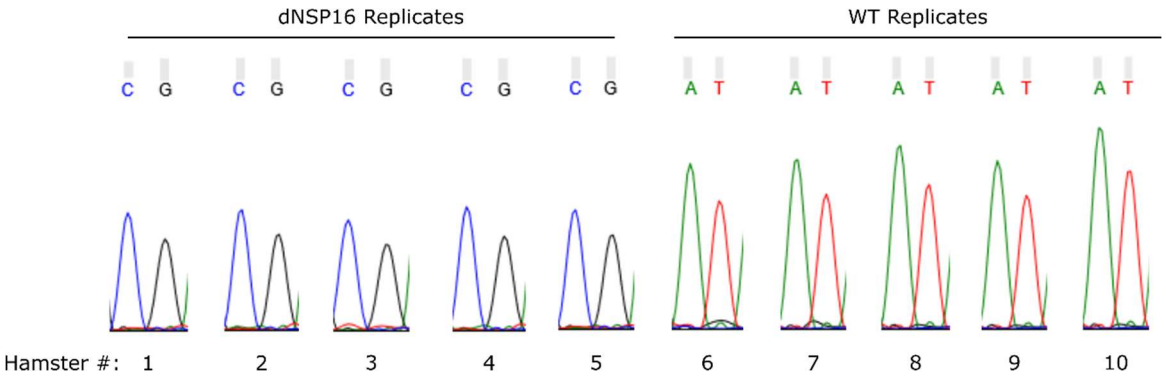

Figure 3.7: No evidence of reversion of dNSP16 mutation was detected *in vivo*.

Viral RNA was extracted from the lungs of hamsters infected with either dNSP16 or WT (numbered 1 through 5 for each group) and which were sacrificed at 4 days post-infection. Viral RNA was reverse-transcribed, PCR-amplified around the site of mutation, and Sanger sequenced. Shown are the sequencing traces of the 2-base pair site within codon 130 of NSP16 that was mutated from AT to CG to engineer dNSP16.

Knockdown of IFIT Genes Partially Reverses Attenuation of dNSP16

Based on increased sensitivity to IFN-I, attenuation of dNSP16 is likely mediated by sensitivity to certain ISG effectors. Therefore, we focused on several ISGs known to target foreign nucleic acids including the IFIT family (*121*), PKR (*122*), and OAS1 (*123*). We transfected Vero E6 cells with target or control siRNAs, treated them with IFN-I, and then infected with either WT SARS-CoV-2 or dNSP16. Whereas control siRNA treatment resulted in undetectable viral titers for dNSP16 at 48 HPI, consistent with the attenuating effect of IFN-I (**Figure 3.3b, c**), we observed a significant restoration of viral titers with anti-IFIT1 siRNA treatment (**Figure 3.8a**). Similarly, siRNA-induced knockdown of IFIT3, shown to stabilize IFIT1 and enhance its cap-binding function (*86*), resulted in a restoration of dNSP16 titers comparable to those observed with anti-IFIT1 siRNA. However, the combination of IFIT1 and IFIT3 knockdown had no additive impact in these studies. Notably, neither anti-PKR nor anti-OAS1 siRNA treatment significantly affected viral replication relative to control siRNA despite confirming knockdown for all targets (**Figure 3.9**). Together, the results suggest that both IFIT1 and IFIT3 play critical roles in the attenuation of dNSP16.

IFIT family members have previously been shown to recognize non-host mRNA cap structures (*124*). Based on the initial siRNA screen (**Figure 3.8a**), we next evaluated if the differences in viral attenuation we noted between dNSP16 and WT SARS-CoV-2 may be due to the presence of baseline IFIT1 expression in the cells we tested. We subsequently observed that Calu-3 2B4 cells expressed IFIT1 protein at baseline, whereas expression of IFIT1 in Vero E6 cells was low (**Figure 3.8b**). However, upon stimulation of Vero E6 cells with IFN-I, we observed a robust induction of IFIT1 that may account for the dNSP16 attenuation we noted (**Figure 3.3c**). We further examined the replication kinetics of dNSP16 in the context of IFIT1 knockdown (**Figure 3.8c**). Whereas treatment with 100 U of IFN-I and control siRNA resulted in undetectable viral titers for dNSP16 at

all time points tested, we observed partial restoration of viral titers for dNSP16 in the context of anti-IFIT1 siRNA treatment at both 24 and 48 HPI (**Figure 3.8c, d**). While the role of IFIT1 has previously been noted for CoV 2'-*O* MTases (*47, 48*), IFIT3 has only recently been shown to enhance IFIT1's RNA-binding ability in human cells (*86*). Similar to IFIT1 knockdown, IFIT3 knockdown restored replication of dNSP16 at both 24 and 48 HPI (**Figure 3.8e, f**). Since IFIT1 and IFIT3 share sequence homology, we also confirmed that both our anti-IFIT1 and anti-IFIT3 siRNA constructs were specific to their respective targets (**Figure 3.10**). Coupled with the fact that combined anti-IFIT1/anti-IFIT3 siRNA treatment had no additive effect (**Figure 3.8a**), these results suggest both IFIT1 and IFIT3 are necessary for attenuation of SARS-CoV-2 dNSP16.

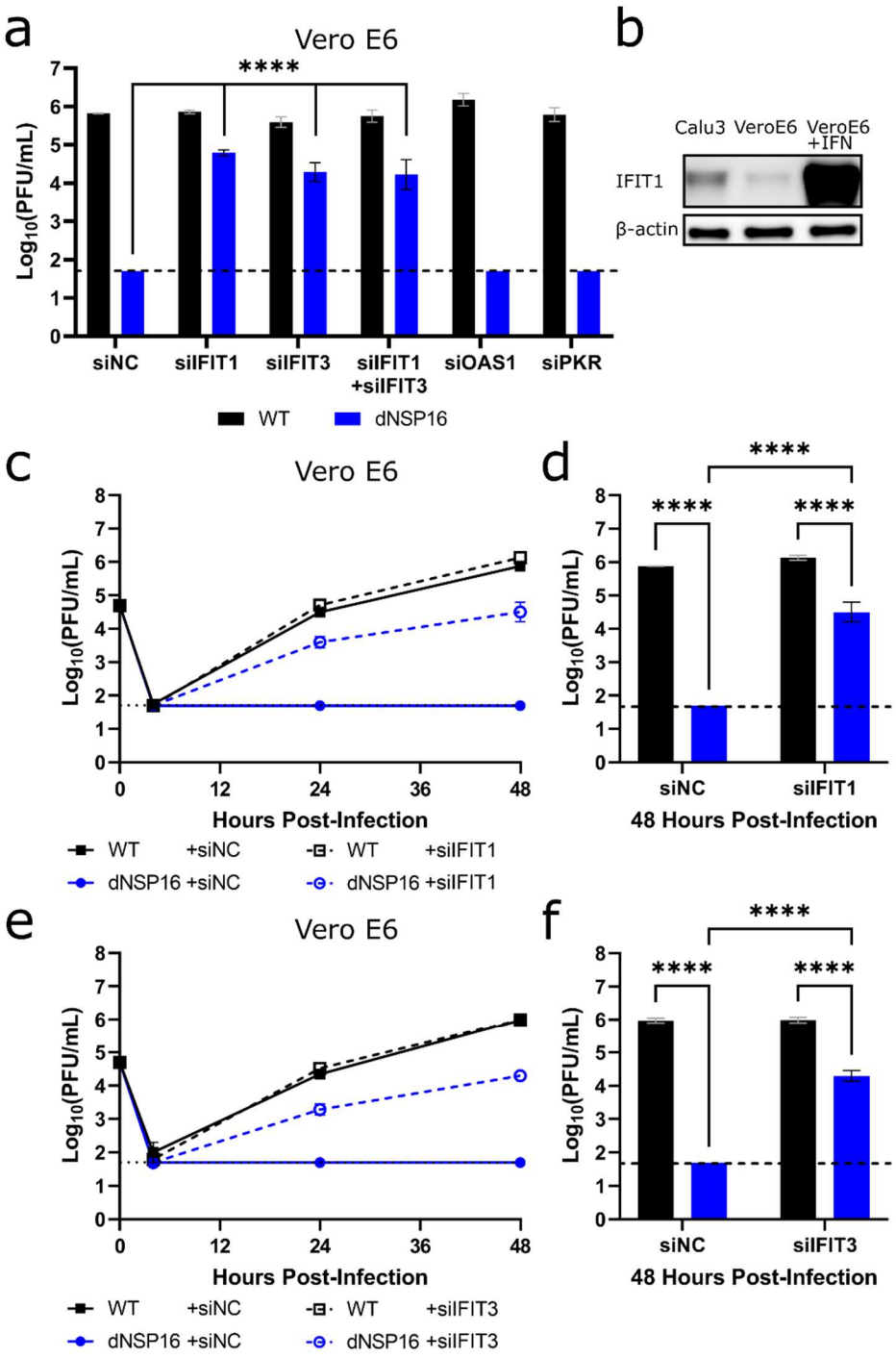

Figure 3.8: Knockdown of IFIT genes partially reverses attenuation of dNSP16.

(a) Replication of WT (black) and dNSP16 (blue) in the context of siRNA treatment. 1.25 x 10^5 Vero E6 cells/well were reverse transfected with 2 pmol total of the indicated siRNA construct(s) 2 days prior to infection and also pre-treated with 100 U IFN-

I a day prior to infection, multiplicity of infection (MOI) = 0.01. Data shown at 48 hours post-infection (HPI). Statistical comparisons on graph are with respect to siRNA control treatment ("siNC"). (b) Baseline IFIT1 protein expression in Calu-3 2B4 and Vero E6 cells, or Vero E6 cells 1 day post-stimulation with IFN-I. (c) Viral replication kinetics for WT (black) or dNSP16 (blue) following treatment with anti-IFIT1 (dashed) or control siRNA (solid). 1.25 x 10^5 Vero E6 cells were reverse transfected with 1 pmol of the indicated siRNA construct 2 days prior to infection and also pre-treated with 100 U IFN-I a day prior to infection, MOI = 0.01. (d) Comparison of the viral titers at 48 HPI from panel (c), black = WT, blue = dNSP16. (e) Viral replication kinetics for WT (black) or dNSP16 (blue) following treatment with anti-IFIT3 (dashed) or control siRNA (solid). 1.25 x 10^5 Vero E6 cells/well were transfected with 1 pmol of the indicated siRNA construct 2 days prior to infection and also pre-treated with 100 U IFN-I a day prior to infection, MOI = 0.01. (f) Comparison of the viral titers at 48 HPI from panel (e), black = WT, blue = dNSP16. For panels (a), (d) and (f), ****$p<0.001$: results of two-way ANOVA with Tukey's multiple comparison test (α = 0.05). Means are plotted with error bars denoting standard deviation. For all panels, n = 3 biological replicates for all data points. Dotted lines represent limits of detection. PFU = plaque-forming units.

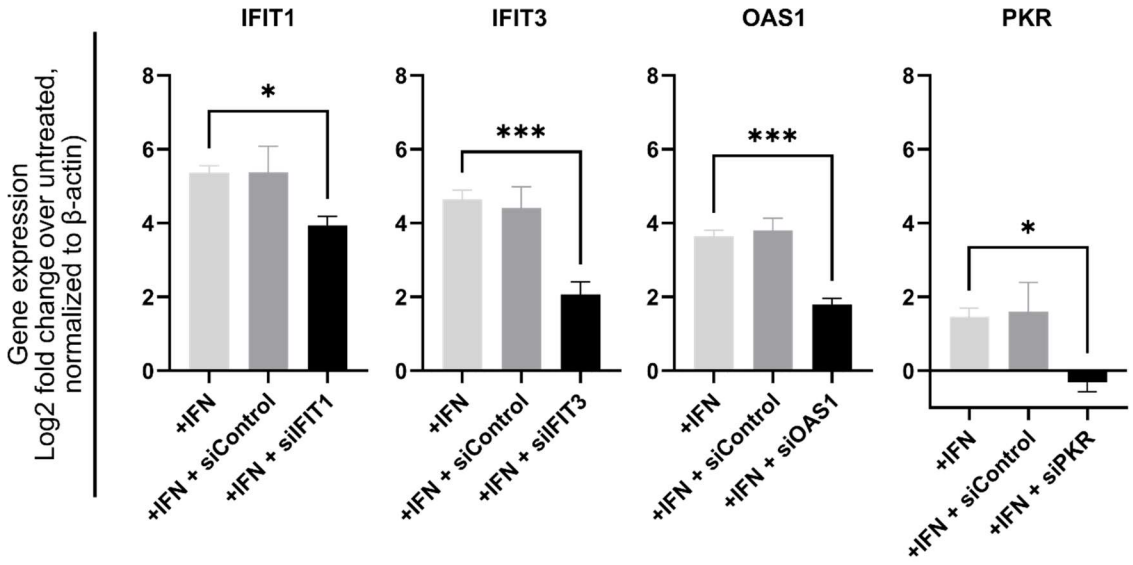

Figure 3.9: Validation of knockdown of immune gene targets in Vero E6 cells.

1.25 x 10^5 Vero E6 cells/well were reverse transfected with 1 pmol of the control or gene-specific siRNA 2 days prior to harvest and also treated with 100 U IFN-I one day prior to harvest and assessment of gene expression. Fold change ($\log_2$) of gene expression is measured relative to untreated samples (*i.e.* no IFN-I). All samples were normalized to β-actin, used as a reference. *p<0.05, ***p<0.005, ns = not significant: results of one-way ANOVA with Tukey's multiple comparison test (α = 0.05). Means are plotted with error bars denoting standard deviation. n = 3 biological replicates.

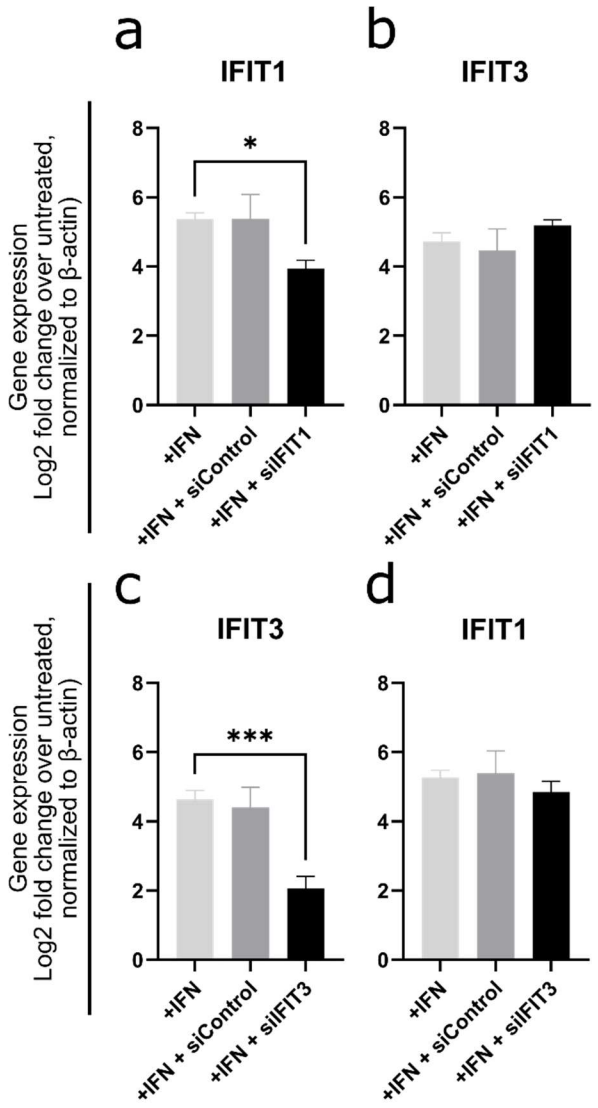

Figure 3.10: Knockdown of either IFIT1 or IFIT3 is specific.

1.25 x 10^5 Vero E6 cells/well were reverse transfected with 1 pmol/well of either a non-targeting siRNA ("siControl") or with an *IFIT1*- (a, b) or *IFIT3*- (c, d) targeting siRNA ("siIFIT1" or "siIFIT3", respectively), or were seeded without treatment. One day later, cells were treated with 100 U of IFN-I to induce interferon-stimulated genes. The following day, cells were lysed for RNA purification and mRNA quantification via reverse transcription and quantitative polymerase chain reaction (PCR). For all panels, gene expression is normalized to *β*-actin (used as a reference), and fold changes are given relative to untreated controls (*i.e.* no IFN). *p<0.05, ***p<0.005, ns = not significant:

results of one-way ANOVA with Tukey's multiple comparison test ($\alpha = 0.05$). Means are plotted with error bars denoting standard deviation. $n = 3$ biological replicates.

Overexpression of IFIT1 Results in Attenuation of dNSP16, which is Augmented by Overexpression of IFIT3

Having shown that IFIT1 and IFIT3 were both necessary for attenuation of dNSP16, we next examined whether IFIT1 or IFIT3 were sufficient for attenuation of dNSP16. We transiently transfected plasmids sharing similar plasmid backbones containing the same CMV immediate early promoter but expressing human IFIT1, human IFIT3, or green fluorescent protein (GFP) as a control. As IFIT1 function has been shown to be enhanced by IFIT3 (*86*), we also tested the combination of IFIT1 and IFIT3, using the same total mass of transfected plasmid as either plasmid alone. We performed transfections in both Vero E6 and the human hepatoma cell line Huh7, and then infected with either dNSP16 or WT. While we did not see differences in Vero E6 cells, likely due to species incompatibility between host cell and ectopically expressed protein(s), we saw a modest, but significant, reduction in dNSP16 replication compared to WT in Huh7 cells overexpressing IFIT1 or IFIT1 in combination with IFIT3 (**Figure 3.11**). WT replication was not affected by any combination of IFIT1 and IFIT3 overexpression, suggesting the ability of WT to evade the antiviral action of IFIT family members. Interestingly, while neither IFIT1 or IFIT3 overexpression had an effect on dNSP16 replication relative to that of the GFP control, the combination of IFIT1 and IFIT3 significantly reduced dNSP16 replication, confirming that IFIT3 enhances the antiviral activity of IFIT1. Together, the results suggest that IFIT1 overexpression is sufficient to attenuate dNSP16, likely due to recognition by IFIT1 of non-host RNA cap structures, and that this IFIT1-mediated attenuation is enhanced by IFIT3.

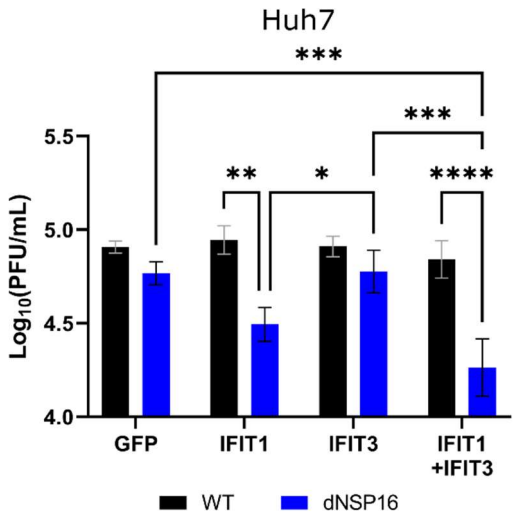

Figure 3.11: Overexpression of IFIT1 results in attenuation of dNSP16, which is augmented by overexpression of IFIT3.

(a) Replication of WT (black) and dNSP16 (blue) in the context of overexpression of IFIT plasmids. 8.5 x 10^4 Huh7 cells/well were reverse transfected with 0.8 µg total of plasmid(s) expressing the indicated protein(s) 2 days prior to infection, multiplicity of infection (MOI) = 0.01. Data shown at 50 hours post-infection (HPI). *p<0.05, **p<0.01, ***p<0.005, ****p<0.001: results of two-way ANOVA with Tukey's multiple comparison test (α = 0.05). Means are plotted with error bars denoting standard deviation. PFU = plaque-forming units.

Targeting the NSP16 Active Site For Antiviral Treatment

Having established the critical role for NSP16 in helping SARS-CoV-2 evade IFIT function, we next explored whether NSP16 activity could be targeted for therapeutic treatment. Using sinefungin, an *S*-adenosyl-L-methionine (SAM) analogue and inhibitor of SAM-dependent MTases (*125*), we attempted to disrupt NSP16 MTase activity and reduce replication of WT SARS-CoV-2. Previous modeling studies demonstrated that sinefungin binds in the active site of NSP16, interacting with the D130 residue we mutated in dNSP16 (**Figure 3.12a**) (*126*). We tested a range of sinefungin concentrations on WT SARS-CoV-2 replication in Vero E6 cells. We observed a dose-dependent decrease in SARS-CoV-2 replication, with 5 mM and 10 mM concentrations reducing replication by 1.6 $\log_{10}$ and 3.1 $\log_{10}$, respectively, compared to mock-treated controls (**Figure 3.12c**, solid bars). However, we also observed an effect of sinefungin treatment on cell viability as measured by ATP production. 5 mM and 10 mM treatment reduced Vero E6 cell viability by 4% and 23%, respectively (**Figure 3.12b**). Moreover, since we did not observe a replication defect with dNSP16 in Vero E6 (**Figure 3.1c**), it is possible that sinefungin, a pan-MTase inhibitor, affected the guanine-N7 MTase function of NSP14 important for viral RNA capping (*127*), or otherwise affected a host cell MTase(s) important for SARS-CoV-2 replication.

While IFN-I treatments (both IFNα and IFNβ) against CoVs have had significant impacts in randomized clinical trials (*31, 128*), our earlier data suggests that disruption of NSP16 activity will sensitize SARS-CoV-2 to IFN-I-induced effectors like IFIT1 and IFIT3. Therefore, we tested the additive impact of sinefungin and IFN-I pre-treatment used in combination (**Figure 3.12c, d**, striped bars). Our results indicated that this combination drove attenuation of WT-SARS-CoV-2 to the replication levels observed with dNSP16 (**Figure 3.3b**). IFN-I treatment alone resulted in a modest, but significant, reduction in titer (1.0 – 1.1 $\log_{10}$), consistent with earlier data (**Figure 3.3b**). However, the addition of

sinefungin to IFN-I pre-treatment resulted in a sinefungin dose-dependent reduction in titer beyond that induced by IFN-I alone. Notably, treatment with 5mM sinefungin and 100 U IFN-I resulted in a 1.9 – 2.6 $\log_{10}$ drop in titer compared to either treatment alone (**Figure 3.12c, d**).

Finally, we tested sinefungin treatment in Calu3 2B4, which are IFN-I competent. As in Vero E6 cells, we observed a dose-dependent decrease in SARS-CoV-2 replication, with 5 mM and 10 mM sinefungin concentrations reducing replication by 1.6 $\log_{10}$ and 1.9 $\log_{10}$, respectively, compared to mock-treated controls (**Figure 3.12f**). Notably, we did not observe a decrease in cell viability in Calu3 2B4 cells due to sinefungin treatment (**Figure 3.12e**). Together, the results argue that targeting NSP16 MTase function in the context of IFN-I signaling may sensitize SARS-CoV-2 to IFN-I-induced effectors and offer a novel approach for therapeutic CoV treatments.

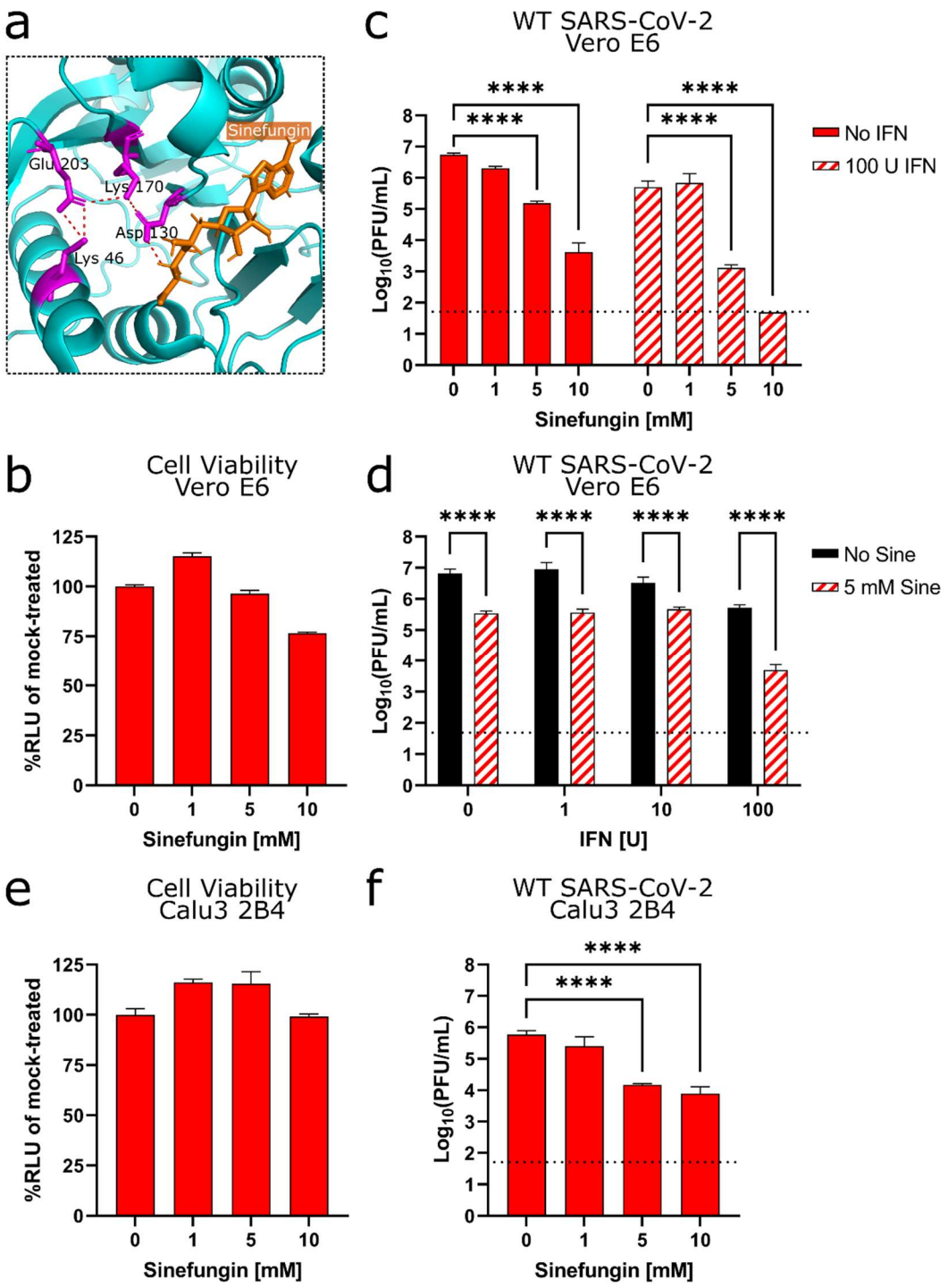

Figure 3.12: Targeting the NSP16 active site for antiviral treatment.

(a) Detail of structure of NSP16 in complex with sinefungin, from Protein Data Bank ID: 6YZ1 (*126*). The residues of the catalytic core are colored in magenta, sinefungin is colored in orange, and polar contacts are shown by orange dashed lines. (b) Cell viability

post-sinefungin treatment as measured by amount of luminescence detected in an ATP detection assay. 1 x 10^3 Vero E6 cells/well were seeded in 96-well format one day before sinefungin treatment. Data shown at 48 hours post-treatment. (c) Dose-dependent effect of sinefungin on WT SARS-CoV-2 replication, with or without IFN-I pre-treatment. 5 x 10^4 Vero E6 cells/well were seeded in 24-well format one day before infection and also pre-treated with 100 U IFN-I 8 hours later. The day of infection (MOI = 0.01), sinefungin was given at the indicated concentration 1 hour after infection (in cell culture media). Data shown at 48 HPI. (d) Dose-dependent effect of IFN-I on WT SARS-CoV-2 replication, with or without sinefungin treatment. 5 x 10^4 Vero E6 cells/well were seeded in 24-well format one day before infection and also pre-treated with the indicated amount of IFN-I 8 hours later. The day of infection (MOI = 0.01), 5 mM sinefungin was given 1 hour after infection (in cell culture media). Data shown at 48 HPI. (e) Cell viability post-sinefungin treatment as measured by amount of luminescence detected in an ATP detection assay. 1.5 x 10^3 Calu3 2B4 cells/well were seeded in 96-well format one day before sinefungin treatment. Data shown at 48 hours post-treatment. (f) Dose-dependent effect of sinefungin on WT SARS-CoV-2 replication. 2 x 10^5 Calu3 2B4 cells/well were seeded in 24-well format five days before infection. The day of infection (MOI = 0.01), sinefungin was given at the indicated concentration 1 hour after infection (in cell culture media). Data shown at 48 HPI. For panels (c) and (d), ****$p<0.001$: results of two-way ANOVA with Tukey's multiple comparison test (α = 0.05). For panel (f), ****$p<0.001$: results of one-way ANOVA with Tukey's multiple comparison test (α = 0.05). For all panels, means are plotted with error bars denoting standard deviation. n = 3 biological replicates for all data points. RLU = relative light units. PFU = plaque-forming units.

Chapter 4 Discussion and Future Directions

Discussion

In this study, we engineered NSP16-mutant SARS-CoV-2 with an amino acid change at a conserved catalytic residue of NSP16, D130A. The mutant, dNSP16, replicated similarly to WT SARS-CoV-2 in the IFN-I-deficient cell line Vero E6, but was attenuated in human respiratory cells. Moreover, dNSP16 showed greater sensitivity to pre-treatment with exogenous IFN-I compared to WT. *In vivo*, dNSP16 was attenuated compared to WT, as evidenced by decreased weight loss, lack of clinical signs of disease, and reduced pathologic changes in the hamster lung. Attenuated disease corresponded to lower viral titers in the nasal wash and lung, as well as reduced viral antigen staining in the lung. Mechanistically, the attenuation of dNSP16 is mediated by IFIT1 and IFIT3, with knockdown of either gene restoring viral replication in the context of IFN-I pre-treatment. Additionally, overexpression of IFIT1, whether alone or in combination with IFIT3, was sufficient to attenuate dNSP16. Lastly, we found that sinefungin, an *S*-adenosyl-L-methionine (SAM) analogue that targets NSP16 activity, reduced WT SARS-CoV-2 replication. In addition, the effect of sinefungin on reducing viral replication was enhanced when combined with IFN-I pre-treatment, likely as a result of decreased NSP16 MTase function and a corresponding increase in recognition by IFIT proteins. Together, our work highlights the critical role of NSP16 in neutralizing the antiviral effects of IFIT1/IFIT3 against WT SARS-CoV-2.

To date, there have been two studies of SARS-CoV-2 NSP16 in the context of live SARS-CoV-2 infection, one focused on antiviral development (*118*), the other focused on attenuated vaccine development (*129*). A third study was published after this dissertation was approved for oral defense, and largely corroborates our findings *in vitro* with regards to IFN-I and IFIT1 sensitivity of a NSP16 2'-*O* MTase mutant SARS-CoV-2 (*130*). While

the mutants described in these published studies contain minor differences in the engineered changes to NSP16 compared to our approach, all of these studies similarly engineered mutations at the D130 codon of NSP16, utilizing either one or two bp changes, with or without also mutating the K170 codon of the catalytic tetrad. A common thread in all four of the NSP16-mutant SARS-CoV-2 studies, including ours, is the attenuation observed *in vitro* in IFN-I competent cell lines. Our study is unique in combining exploration of mechanisms of attenuation *in vitro* with a pathogenesis study in the hamster model, allowing direct comparisons of pathogenic results *in vivo* with mechanistic insights *in vitro*. Our study also adds novel data to the field in highlighting the role of IFIT3 in mediating attenuation of NSP16-mutant SARS-CoV-2, underscoring the synergistic role of IFIT1 and IFIT3 in antagonizing NSP16-mutant SARS-CoV-2, and measuring the effects of sinefungin on SARS-CoV-2 replication.

In our study, we observed that ablating NSP16 MTase activity does not result in loss of the replicative capacity of dNSP16 compared to WT in IFN-I-incompetent cells. Yet, our inability to rescue an NSP16-deletion virus with an inserted stop codon suggests NSP16's role may be more complex than its 2'-*O* MTase activity alone. Notably, replication attenuation of dNSP16 occurs in the context of a viable IFN-I response. These results are consistent with previous studies of 2'-*O* MTase mutants in CoVs including SARS-CoV (*47*) and MERS-CoV (*48*). Similarly, reduced disease and attenuation of viral replication at 4 DPI in the lung of dNSP16-infected hamsters is consistent with data from other 2'-*O* MTase CoV mutants in mouse models (*47, 48*). However, our viral titer data from nasal washes, a measure of viral fitness in the upper airway, indicate that dNSP16 attenuation occurs at the earlier 2 DPI time point. These results, not surveyed in the CoV mouse models, suggest the upper airway and the lung have distinct immune activation responses, leading to different kinetics for dNSP16 attenuation.

Our studies also confirm a role for the IFIT proteins in mediating attenuation of dNSP16. Previously, human IFIT1, an ISG, has been shown to sequester viral mRNA

lacking 2'-*O* methylation (*93*) through a mechanism that involves direct recognition of the cap structure (*131*). In prior studies with CoVs, mouse Ifit1, paralogous to human IFIT1 (*132*), antagonized CoVs lacking 2'-*O* methylation (*49, 50*). Here, we demonstrate that while dNSP16 is attenuated by IFN-I pre-treatment in Vero E6 cells, knockdown of IFIT1 partially restores dNSP16 replication. In addition, rapid attenuation of dNSP16 in Calu-3 2B4 cells, compared to Vero E6 cells, may be due to higher baseline levels of IFIT1 in the former. We also found that knockdown of IFIT3 partially restored dNSP16 replication in the context of IFN-I pre-treatment. Recent studies have highlighted the importance of IFIT3 in stabilizing IFIT1 function and optimizing its recognition of RNA caps lacking 2'-*O* methylation (*86*). Notably, the combination of IFIT1 and IFIT3 knockdown we tested had no additive effect, suggesting that both together are required for restriction of dNSP16. Conversely, we found that the combined overexpression of IFIT1 and IFIT3 was sufficient for attenuating dNSP16, and had a stronger effect than overexpression of IFIT1 alone. Overall, our results indicate the importance of NSP16 in protecting SARS-CoV-2 from IFIT effector function.

Having established a critical role for NSP16 in evading IFIT activity, we evaluated the feasibility of targeting 2'-*O* methylation of CoVs therapeutically. Using sinefungin, a pan-inhibitor of SAM-dependent MTases, we observed a dose-dependent reduction in replication of WT SARS-CoV-2, indicating that targeting NSP16 activity can impair successful infection. Importantly, combined treatment with sinefungin and IFN-I had an additive effect, resulting in increased attenuation. A similar, synergistic effect was recently observed with the SAM cycle inhibitor 3-deazaneplanocin A (DZNep) and IFN-I (*118*). This is likely due to both a loss of viral 2'-*O* methylation (i.e. cap1) and increased recognition of unmethylated viral RNA (i.e. cap0) by IFIT1/IFIT3. Targeting NSP16 MTase function involves a host-directed mechanism distinct from those of other CoV therapies targeting the viral polymerase (*133*) or the main protease (*134*) to arrest virus replication. Targeting NSP16 similarly disrupts a viral enzymatic process; yet here, an

effector response is provided by the host via IFIT functions. Importantly, while attenuation of dNSP16 is delayed in the hamster lung, early attenuation in the upper airway suggests more rapid or robust expression of IFIT proteins in the upper airway. This could, in turn, increase the efficacy of drugs targeting CoV 2'-*O* MTase activity in the upper airway, a possible strategy to decrease transmission. With augmented upper airway replication a feature of SARS-CoV-2 variants of concern (*46*), NSP16-targeting drugs may provide an effective countermeasure for the current and future CoV pandemics.

Overall, our results confirm the importance of NSP16 to SARS-CoV-2 infection and pathogenesis. A mutation that disrupts the NSP16 2'-*O* MTase catalytic site attenuates disease *in vivo* and demonstrates its importance in evading host innate immunity. In the absence of 2'-*O* MTase activity, SARS-CoV-2 is rendered susceptible to the effector responses of IFIT1 and IFIT3 in combination. Importantly, such dependence of SARS-CoV-2 on the 2'-*O* MTase function of NSP16 offers a novel target for future CoV antiviral drug development.

Future Directions: Targeting NSP16 MTase Function

In light of recurrent epidemic cycles of SARS-CoV-2, and the tendency of new variants of concern to emerge, there is a continued need for development of antiviral treatments. The development of antivirals that target 2'-*O* MTase function could be a useful tool in a steadily growing arsenal of SARS-CoV-2 antiviral therapies (*135*). A SARS-CoV-2 NSP16 MTase inhibitor could perhaps synergize with other antivirals, as seen with synergy between the nucleoside analog remdesivir and the 3C-like protease inhibitor nirmatrelvir (Paxlovid) (*136*), and with remdesivir and a SAM cycle inhibitor (*118*).

Given the importance of 2'-*O* MTase function to viruses, and the availability of viral MTase structural data (*102*), including structural data for SARS-CoV-2 NSP16 (*60,*

113, 126, 137), MTase function would appear an attractive target for antiviral drug development (*68*). Antiviral drug development for emergent CoVs in general has typically relied on repurposing drugs originally designed for other pathogens, such as the nucleoside analogs remdesivir (*138*) and molnupiravir (*133*). However, in the case of nirmatrelvir (Paxlovid), an anti-CoV NSP5 (3C-like protease) compound was originally developed against SARS-CoV but shelved when SARS subsided. Development resumed after the emergence of SARS-CoV-2 (*139*). The antiviral drug development pipeline is an iterative process that typically begins with examining the structure-activity relationship (SAR) of a candidate inhibitor compound, perhaps identified from a high-throughput screen, before synthesizing optimized ligands based on SAR analysis, performing binding assays, solving the co-crystal structures of ligand bound to target, and modifying secondary chemical moieties to improve parameters such as solubility and cell permeability that affect the pharmacokinetic profile of a compound. Candidate compounds are tested for antiviral potency, as well as potential toxicity, both *in vitro* and in preclinical models *in vivo* (*136, 139*). Promising candidates may move onto clinical trials, but this is not guaranteed given the substantial costs associated with them (*140*).

Modeling the binding of potential inhibitors to NSP16 can, in principle, screen up to millions of commercially available compounds in simulated binding studies *in silico*. For viral MTases, these studies examine compounds that bind either the SAM site or the RNA cap site (*141*), or both (*127*) in a bi-substrate mechanism of action. Such studies can also model the likelihood of cross-reactivity to host MTases. Subsequent to molecular modeling *in silico*, both cell-based and cell-free screening methods could help identify compounds active against NSP16, each method conferring its own advantages (*68*). Cell-free methods rely on purified components and provide more direct evidence of interaction, while cell-based methods typically assay antiviral activity in the context of viral replication and therefore represent a more relevant biological context. The two methods should be used complementarily to establish both the specificity and antiviral potency of candidate

antiviral inhibitors. Once identified and validated for effectiveness *in vitro* and *in vivo*, candidate NSP16 inhibitors would likely need to be further optimized to satisfy drug development benchmarks.

Thus far, methods for high-throughput screening of compounds against NSP16 have been published (*142*) and also employed (*118*). While screens for antivirals against NSP16 in the context of viral replication have been few in number, one recent study models a comprehensive approach (*118*). This study highlights the drug discovery process described above: modeling efforts *in silico* identified several compounds with potential activity against NSP16; these compounds were then screened in a cell-free assay for specificity against NSP16 MTase function; finally, compounds that exhibited inhibitory activity were screened in a cell-based assay against SARS-CoV-2 replication. The study identified the adenosine analog tubercidin as a compound with both specificity toward NSP16 MTase activity as well as effectiveness against SARS-CoV-2 replication. Finally, the same study tested tubercidin in a preclinical mouse model of SARS-CoV-2 infection. While the compound reduced viral load in the lung, it also resulted in greater toxicity as measured by increased weight loss.

The tubercidin study also highlights the possibility that SARS-CoV-2 may rely on, or at least be able to utilize when necessary, a host 2'-*O* MTase, an overlooked aspect of our own study. Consistent with our findings, NSP16-mutant SARS-CoV-2 replication in IFN-I-competent ACE2-expressing A549 (A549-ACE2) cells was reduced compared to WT. However, in the context of knockout of CMTR1, a host 2'-*O* MTase previously known to be induced by IFN-I (*143*), the NSP16-mutant was even more attenuated (*118*), suggesting SARS-CoV-2 may utilize a host 2'-*O* MTase when necessary. The reliance of viruses on host 2'-*O* MTases has precedent: HIV-1, which does not encode a 2'-*O* MTase, recruits the host 2'-*O* MTase FTSJ3 to methylate viral RNA (*69*). In the case of SARS-CoV-2, it remains to be seen whether the virus actively recruits CMTR1 or other host MTases to viral RNA in order to effect 2'-*O* methylation of viral RNA.

The sinefungin data presented in our work suggests sinefungin is indeed active against viral replication; however, we did not thoroughly examine off-target effects, especially against host MTases. Nevertheless, a rationally designed inhibitor of 2'-*O* MTase function specific to CoVs could potentially reduce or eliminate the possibility of cross-reactivity against host MTase function. Additionally, the effective antiviral concentration of sinefungin we observed in our study was high, in the millimolar range. Studies of potential inhibitors of SARS-CoV-2 NSP14 guanine-N7 MTase have identified compounds in the sub-micromolar IC_{50} (*127*) and even nanomolar IC_{50} range (*144*). A tailor-made inhibitor of NSP16 2'-*O* MTase function could perhaps achieve comparable inhibitory potency.

In addition to inhibitors that directly inhibit NSP16 function, other compounds that interfere with the SAM cycle may also represent an indirect means to interfere with NSP16 activity. One such compound, 3-deazaneplanocin A (DZNep) inhibits *S*-adenosyl-L-homocysteine hydrolase, responsible for catabolizing *S*-adenosyl-L-homocysteine, the byproduct of SAM and a competitive inhibitor of MTases (*145*). Two studies have demonstrated the inhibition of SARS-CoV-2 by DZNep *in vitro* (*118, 146*), and one study has also shown reduced viral titer in the lungs of mice administered DZNep intranasally in two doses, one hour and one day post-intranasal challenge (*118*). In the latter study, DZNep was also shown to synergize with IFNα and remdesivir *in vitro*, demonstrating the potential of deploying a SAM cycle inhibitor alongside other antiviral medication or, consistent with our own findings of the additive effect of sinefungin and IFN-I, in the context of endogenous IFN-I expression.

Because of the likely synergy between NSP16 MTase inhibitors and IFN-I, NSP16 MTase inhibitor treatment *in vivo* may be particularly promising. We observed dNSP16 was more highly attenuated in nasal wash as opposed to the lung, suggesting, perhaps, increased IFN-I signaling in the nasal passages. If true, development of a nasal spray containing an NSP16 MTase inhibitor could be attractive therapeutic approach, which

could be deployed either prophylactically or therapeutically to limit SARS-CoV-2 replication in the upper airway, possibly reducing both COVID-19 symptoms and transmission. In the hamster model, SARS-CoV-2 replication was particularly robust in the nasal turbinates, even in the context of neutralizing antibody treatment that effectively reduced viral load in the lung (*147*). Therefore, targeting SARS-CoV-2 replication in the nasal passages with an NSP16 MTase inhibitor may give a unique advantage over other treatments.

In addition to targeting the NSP16 MTase with antiviral therapeutics, targeting the NSP10-NSP16 interface is another possible approach to abrogate NSP16 function. NSP10 is required for NSP16 binding to both RNA substrate and SAM (*148*), and therefore, blocking the interaction of NSP16 with NSP10 would preclude NSP16 MTase function. Indeed, this strategy was employed in a study of MHV, in which a ~30 amino acid peptide was designed to target the NSP16-binding domain of NSP10. Treatment *in vitro* reduced MHV replication (*149*). Moreover, the NSP10 peptide, which was covalently linked to a cell-penetrating moiety derived from HIV-1 Tat protein, was also able to prevent mortality and morbidity from MHV infection when administered intrahepatically to mice. For our study, we designed a SARS-CoV-2-specific NSP10 peptide with amino acid sequence spanning amino acids 4321 – 4349 of ORF1a, a critical region of the NSP16-binding interface of NSP10 (*113*). We appended the same cell-penetrating HIV-1 Tat protein as described in (*149*) to the N-terminus of the peptide. We observed a modest (<0.25 $\log_{10}$) effect on viral replication in the context of IFN-I pre-treatment, compared to a scrambled control peptide (**Figure 4.1**), suggesting disruption of binding of NSP10 to NSP16 sensitized the virus to cap-sensing IFN-I effectors such as the IFIT family proteins. However, both the NSP10 peptide and scrambled peptide reduced viral titer by ~ 2.0 $\log_{10}$ relative to vehicle controls, suggesting any antiviral effect we may have observed for our NSP10 peptide was mild compared to a strong non-specific effect resulting from peptide treatment itself. While we did not explore ways to overcome this limitation, it is clear that

candidate peptide-based inhibitors of NSP10-NSP16 interaction need to carefully control for non-specific effects.

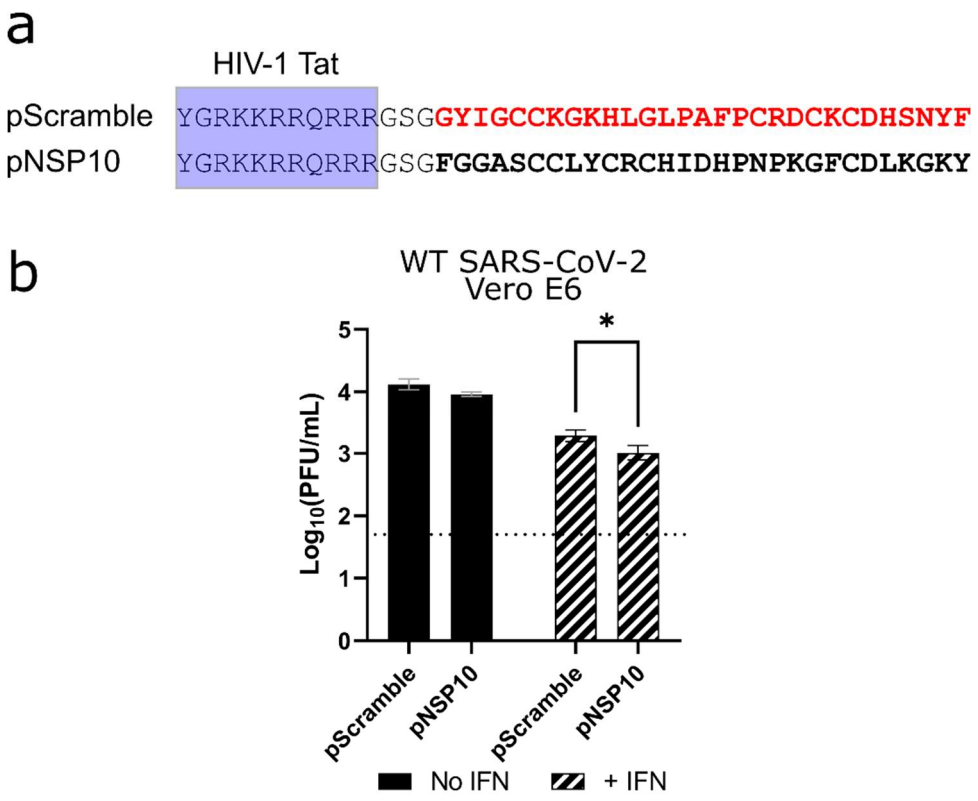

Figure 4.1: WT SARS-CoV-2 replication is reduced by treatment with NSP10 peptide relative to a scrambled control peptide.

(a) Peptide design. Bolded region of pNSP10 sequence corresponds to amino acids 68 – 96 of SARS-CoV-2 NSP10. The same sequence is scrambled in pScramble. HIV-1 Tat sequence is shaded in blue. (b) Effect of peptide treatment on WT SARS-CoV-2 replication, with or without pre-treatment of IFN-I (2 U). 1.5 x 10^3 Vero E6 cells/well were seeded in 96-well format, and treated with IFN-I (or mock-treated) 6 hours after. The next day, cells were infected with WT SARS-CoV-2 (MOI: 0.1). At 1 HPI, cells were treated with 100 µM of either peptide. Data shown at 24 HPI. Means are plotted with error bars denoting standard deviation. *p<0.05: result of two-way ANOVA with Tukey's multiple comparison test (α = 0.05). n = 3 biological replicates for all data points. PFU = plaque-forming units.

NSP16-Deficiency as a Basis for Live Attenuated Vaccines

In addition to presenting an attractive target for antiviral development, NSP16 could also be the basis for live attenuated vaccine (LAV) development. NSP16-mutant SARS-CoV protected mice from lethal challenge with WT virus, when administered as a 10^2 PFU dose intranasally four weeks before challenge with 10^5 PFU WT virus (*47*). Similarly, NSP16-mutant MERS-CoV protected mice from lethal challenge with WT virus, when administered as a 10^6 PFU dose intranasally four weeks before challenge with 10^6 PFU WT virus (*48*). In both these studies, serum neutralizing antibody titer induced by vaccination (or present after challenge) correlated with protection. Recently, an NSP16-deficient mutant of SARS-CoV-2 administered intranasally in a 10^5 PFU dose was shown to protect hamsters challenged with a 10^5 PFU dose of a clinical SARS-CoV-2 isolate and even afforded sterilizing immunity as evidenced by undetectable viral titer in both the lung and nasal wash, which correlated with neutralizing serum antibody detectable at 7 DPI (*129*). For our study of infection of dNSP16 and WT in hamsters, we also measured serum neutralizing antibody titer at 7 DPI. While serum from WT-infected hamsters displayed the highest neutralization potential, serum from dNSP16-infected hamsters did display higher neutralization potential compared to that of mock-infected hamsters (**Figure 4.2a**). The trend we observed was consistent with serum neutralizing antibody titer in hamsters at 7 DPI from a recent study of a different attenuated mutant of SARS-CoV-2 (*150*). In that study, which utilized a mutant SARS-CoV-2 deficient in ORFs 3, 6, 7, and 8, serum neutralizing antibody titer from WT-infected hamsters was also higher than that of mutant-infected hamsters at 7 DPI.

To aid LAV development, comparisons of correlates of protection elicited by dNSP16 compared to other attenuated mutants would be worthwhile (**Figure 4.2b**). Combination of the NSP16-D130A mutation with other attenuating mutations may also reduce the risk of reversion to full pathogenicity (*151*). To that end, we are currently

engineering a mutant of SARS-CoV-2 with the NSP16-D130A mutation as well as deletion of the QTQTN motif (Δ675 – 679) of the spike gene upstream of the furin cleavage site, which attenuates SARS-CoV-2 pathogenesis (*44*). A LAV strategy utilizing combination attenuation has been studied for SARS-CoV in a preclinical model (*151*). Such an approach, involving both the NSP16-D130A mutation as well as two alanine substitutions (D90A/E92A) in the exonuclease domain of NSP14, provided heterologous protection, protected against age-dependent disease, and prevented reversion to virulence. In summary, NSP16 deficiency attenuates SARS-CoV-2, as well as other CoVs, and could contribute to a LAV strategy against CoVs.

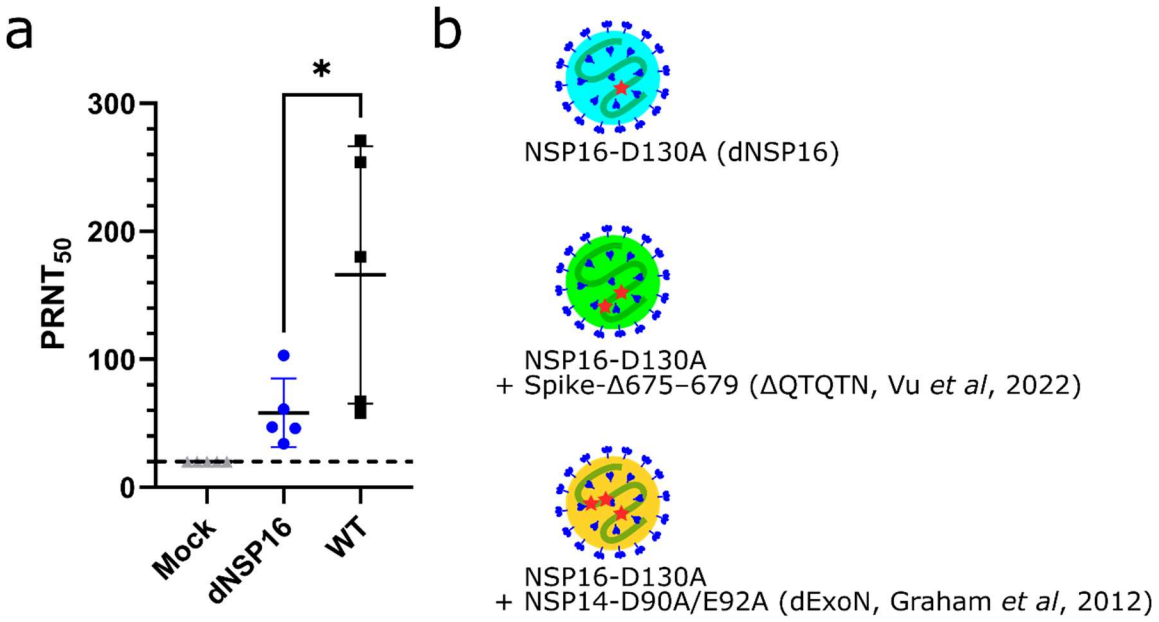

Figure 4.2: dNSP16 induces serum neutralizing antibody at 7 days post-infection

(a) Neutralizing antibody titer against WT SARS-CoV-2, from serum of hamsters included in the study outlined in Figure 3.4: a 100 µL inoculum of PBS (mock) or either dNSP16 (10^4 plaque-forming units) or WT (10^4 plaque-forming units) was given intranasally to 4- to 5-week-old Syrian hamsters. Serum was collected at 7 days post-infection. Y-axis denotes the interpolated serum dilution factor that resulted in 50% reduction of plaque counts ($PRNT_{50}$), relative to serum-free control. Each data point denotes value from one hamster and represents the mean of two technical replicates. Means plotted as horizontal black lines, with standard deviation shown. *p<0.05: result of two-tailed unpaired t-test (α = 0.05). Dotted line represents limit of detection. (b) LAV candidates for SARS-CoV-2. For LAV design, the NSP16-D130 of dNSP16 (top) may also be included with other mutations described in the literature, namely the attenuating Spike-(Δ675 – 679) mutation described in (*44*), or the NSP14-D90A/E92A mutation described for SARS-CoV, which was tested in combination with NSP16-D130A for SARS-CoV (*152*). We are close to rescuing the middle virus depicted.

Exploring Other Roles of NSP16

While we have focused on the MTase function of NSP16, NSP16 may have other roles that warrant additional exploration, and perhaps further justify developing antiviral therapeutics targeting NSP16. NSP16 binds U1 and U2 small nuclear RNAs (snRNAs) to disrupt splicing of host mRNAs (*153*). This interaction is likely mediated by the RNA binding site of NSP16, but the physical basis for this interaction remains to be explored, as well as whether MTase function is dispensable for this interaction. Interestingly, NSP14 MTase activity was suggested to be necessary for host translational shutdown (*154*). The role of NSP16 in CoV replication likely extends beyond its MTase function. Because we did not detect replication of SARS-CoV-2 engineered with a stop codon within NSP16, NSP16 may be a necessary component of the RTC, although the nature of this necessity remains to be fully characterized. There is preliminary evidence that NSP16 can form a trimer complex with both NSP10 and NSP14, and that this interaction modulates the exonuclease activity of NSP14 (*155*). Thus, it appears likely that NSP16 may be essential to aspects of the CoV RTC outside of its function as the 2'-*O* MTase for CoVs. Further dissection of these aspects to NSP16 function should help light the way to understanding CoV pathogenesis and designing better treatments against it.

Appendix: Anti-IFIT1 Treatment *In Vivo*

Treatment with an Anti-IFIT1 Morpholino in Hamster Differentially Affects Replication of dNSP16 and WT.

Given the effect of IFIT1 knockdown on the replication of dNSP16 *in vitro* (**Figure 3.8**), we sought to probe the interaction of dNSP16 and IFIT1 *in vivo*, using the same animal model we had used prior (**Figure 3.4**). Although the IFIT1 paralogs of Syrian hamster are "predicted" sequences as annotated in NCBI GenBank, we did confirm expression of three IFIT1 paralogs in the hamster lung (**Figure A.1b**). We designed a translation-blocking antisense morpholino targeting the upstream 5' untranslated region of one of three annotated IFIT1 paralogs in Syrian hamsters (**Figure A.1c**). We chose the morpholino sequence based on homology of the target hamster IFIT1 paralog to murine IFIT1 (**Figure A.1a**), because prior studies had shown restoration of MTase mutants in IFIT1$^{-/-}$ mice (*47, 49*). We first validated the efficacy of the anti-IFIT1 morpholino in BHK cells which are derived from Syrian hamster (*156*). The anti-IFIT1 morpholino induced a partial knockdown of IFIT1 protein levels in BHK cells (**Figure A.2a**), as evidenced by protein detection using a polyclonal anti-mouse IFIT1 antibody, although we did not confirm which paralog(s) were knocked down. We administered the anti-IFIT1 morpholino, or a non-targeting morpholino control, to hamsters in two i.n. doses at 2- and 1-day prior to infection, and then infected i.n. with 10^4 PFU of either dNSP16 or WT (**Figure A.2b**). While we did not observe morpholino-induced changes in weight loss over the 7-day period post-infection (**Figure A.2c**), we did observe a morpholino-induced difference in viral titer in nasal washes at 2 DPI (**Figure A.2d**). Whereas control morpholino-treated hamsters did not show a difference at 2 DPI, anti-IFIT1 morpholino-treated, WT-infected hamsters had higher viral titer in the nasal wash compared to anti-IFIT1 morpholino-treated, dNSP16-infected hamsters, suggesting a NSP16-dependent effect. We did not observe a similar difference in titer in the nasal wash at 4 DPI (**Figure**

A.2e), nor in the lung at either timepoint. We also measured protein levels of IFIT1 in the lung at 2 DPI, but did not observe differences between anti-IFIT1- and control morpholino-treated hamsters. While the results of anti-IFIT1 morpholino treatment *in vivo* did not corroborate our findings *in vitro* (**Figure 3.8**), they may suggest additional antiviral properties of IFIT1 that are not specific to 2'-*O* methylation, as knockdown of IFIT1 differentially increased WT titer over dNSP16 titer in the nasal wash at 2 DPI, compared to control morpholino treatment. Importantly, our results also suggest that targeting knockdown of only one of the three IFIT1 paralogs in Syrian hamsters is insufficient to restore the attenuation of dNSP16 *in vivo*. Future experiments with more thorough knockdown of IFIT1 paralogs in hamsters, or, alternatively, knockdown of IFIT1 in a mouse model of SARS-CoV-2 infection, such as K18-hACE2 transgenic mice (*157*), may yield results more consistent with prior studies using IFIT1$^{-/-}$ mouse models of CoV infection (*47*).

a

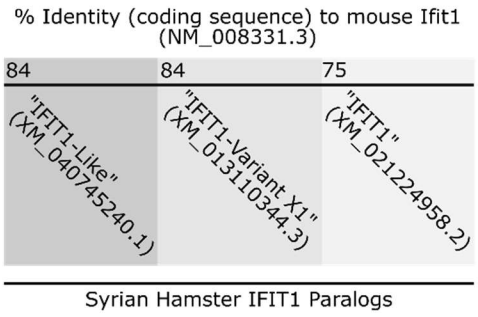

b

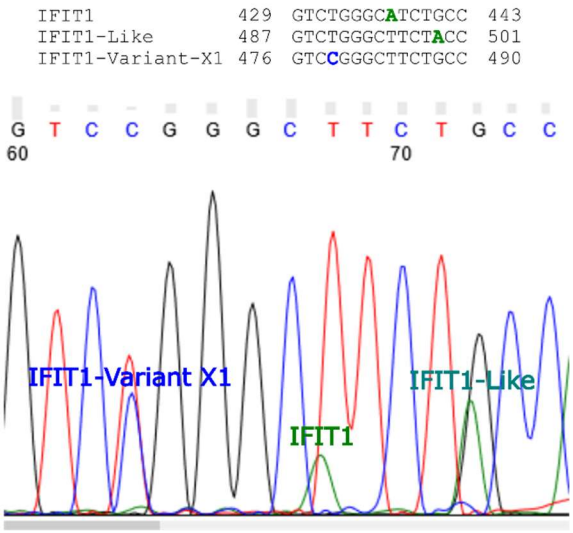

c

```
IFIT1                ---------------------------------------------CTGTACATGAATACCT 16
IFIT1-Like           GTGACAGCAAGAGCACATCACAGCTCACAGAGCTGCTTCCCAGCCCTTATATGAGAGTCC 60
IFIT1-Variant-X1     ---------AGAACTTATCACAGCTCACAGAACTGCTTCCCAGCCTTTATA--TGAGTCC 49
                                                     *  ** *       *

IFIT1                TGTTTATTTGAGA----ACCAACCC--CTAGA-ACCCCATTGAATTTGGAAGAGCCT--- 66
IFIT1-Like           ACAGGGTGAGAAAGTCCACTAGACAGCAGAGAGTCAAGGCAGAATTCTGAAGAGCACTAT 120
IFIT1-Variant-X1     AGGCAGTGAGAAAGTCCCCCAGATAGCAGAGCTTCAAGGTGGGATTCTGAGGAGCCCTAT 109
                           *  ** *     * *        **   *      * ***  ** ****

IFIT1                CTTGGCCT-GAATCAAAGTACTAAGGAGCTGTCTCCCAGCAACATGAGTGAAGAGTCTCA 125
IFIT1-Like           CCTGGTAAAATCCCAGACAACTGCTGCCACCTTCACAGCAACTATGGGAGACCATGCTGG 180
IFIT1-Variant-X1     CCTGTTGAAAACCCAGTCAACTGCTACCACCTTCACAGCAACCATGGGAGACCATGCTGG 169
                     * **         **    ***         *   *    *  *** * **  *  **

IFIT1                TAGAAATCCCATGCTGGAAAATCTGCTTCAGCTGAGATGTCACTTTACTTGGGAGTTGCT 185
IFIT1-Like           TGATGCCCAGGTGGAGGAGAAGCTGCTTCAGCTGAGATGTCACTTCACATGGGGACTGCT 240
IFIT1-Variant-X1     TGATGCCCAGGTGGAGGAGAAGCTGCTTCAGCTGAGATGCCACTTCACATGGGGACTGCT 229
                     *      *   **  *** ** ***************** ***** ** ****   ****
```

Figure A.1: Designing an IFIT1-targeting morpholino for use *in vivo*.

(a) Percent nucleotide identity of the coding sequences of three IFIT1 paralogs in the Syrian hamster NCBI GenBank-annotated genome to murine Ifit1. (b) Sequencing of RNA reverse transcribed and amplified from hamster lung confirms expression of three distinct paralogs of IFIT1. Top panel shows alignment of a short region of sequences sourced from the respective GenBank records, with paralog-specific single nucleotide polymorphisms bolded. Bottom panel shows Sanger sequencing trace of reverse-transcribed and PCR-amplified hamster lung RNA, with peaks corresponding to each paralog labeled. (c) Alignment of the 5' untranslated regions and upstream coding

sequences of NCBI GenBank-annotated hamster IFIT1 paralog sequences. Start codons are bolded. Asterisks represent identity across all three sequences. Solid underline represents the target of the designed morpholino, specific to IFIT1-Like. Dotted underline represents probable cross-specificity of the morpholino to IFIT1-Variant-X1. Two mismatches are colored red. Note, that the gap in sequence alignment of IFIT1-Variant-X1 to IFIT1 does not affect morpholino specificity.

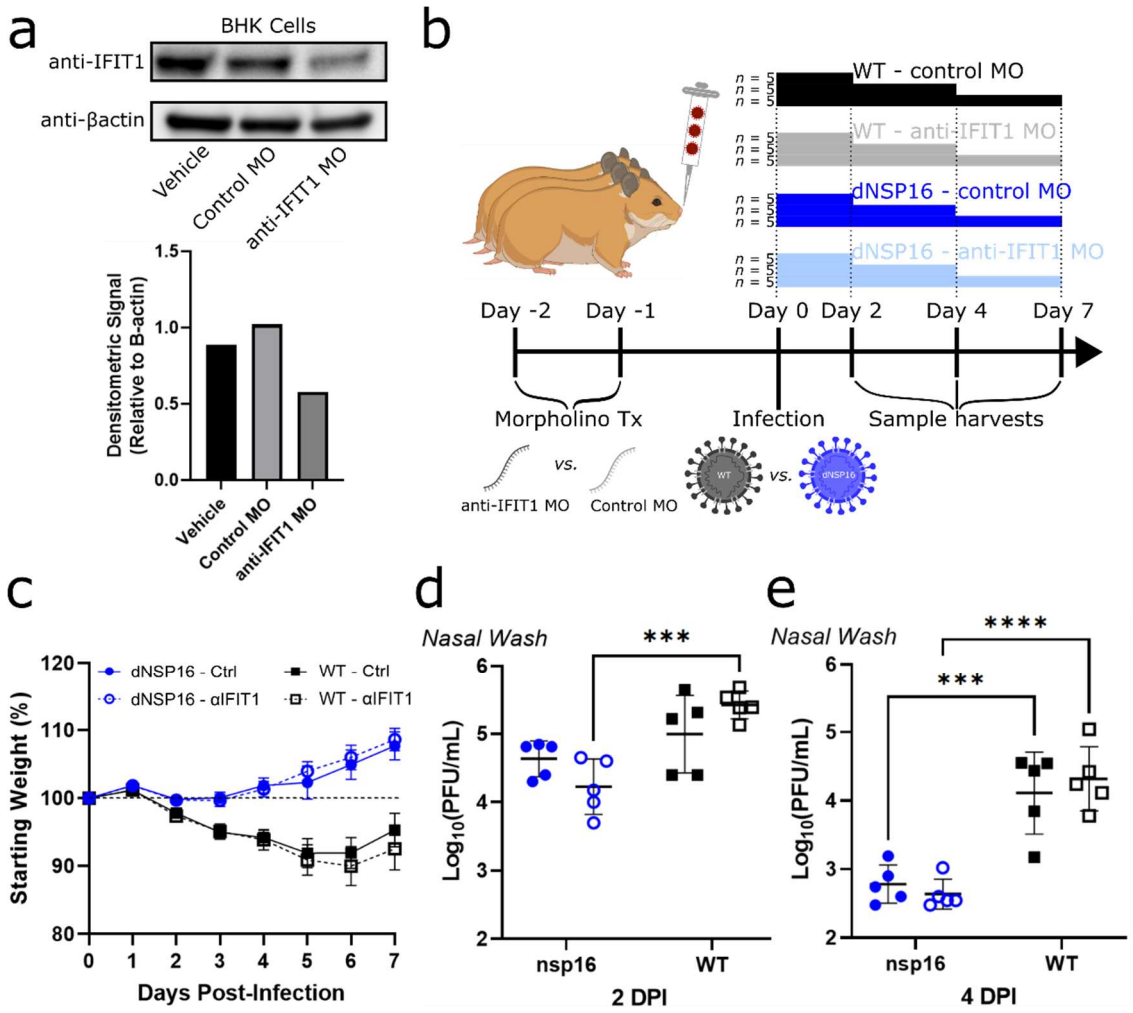

Figure A.2: Treatment with an anti-IFIT1 morpholino in hamster differentially affects replication of dNSP16 and WT.

a) Validation of anti-IFIT1 morpholino in baby hamster kidney (BHK) cells. Control or anti-IFIT1 morpholino ("MO") or no morpholino ("Vehicle") was supplied in growth medium at 10 µM to BHK cells. One day later, 750 U of IFN-I was added to cells, and after an additional two days, cells were harvested for protein expression via western blot. IFIT1 levels were assessed via polyclonal anti-mouse IFIT1 antibody and signal levels were normalized against β-actin, used as a reference, bottom panel. (b) Overview of experimental plan of morpholino treatment and subsequent viral infection. 370 ng (36 nmol) of sterile water-dissolved control or anti-IFIT1 morpholino in a 72 µl inoculation volume was administered intranasally (i.n.) to 4- to 5-week-old Syrian hamsters at 2- and

1-day prior to infection. On the day of infection, a 100 μL inoculum of either dNSP16 (10^4 plaque-forming units or PFU) or WT (10^4 PFU) was given i.n. At 2, 4, and 7 days post-infection (DPI), 5 animals from each infection group were sacrificed for organ collection. (c) Percent starting weights over time for control ("Ctrl") or anti-IFIT1 ("αIFIT1") morpholino-treated, and either dNSP16- or WT-infected hamsters. (d) Comparison of viral titers from nasal washes at 2 DPI. (e) Comparison of viral titers from nasal washes at 4 DPI. For panels (d) and (e), values from individual hamsters are plotted (symbols) as well as means (bars). Error bars denote standard deviation. ***$p<0.005$, ****$p<0.001$: results of two-way ANOVA with Tukey's multiple comparison test ($\alpha = 0.05$). Adapted from "Hamster (lateral)," "unwound ssDNA brush (wavy," and "SARS" by BioRender.com (2022). Retrieved from https://app.biorender.com/biorender-templates.

References

1. C. Schindewolf *et al.*, SARS-CoV-2 Uses Nonstructural Protein 16 to Evade Restriction by IFIT1 and IFIT3. *bioRxiv : the preprint server for biology*, (2022).
2. COVID-19 Excess Mortality Collaborators, Estimating excess mortality due to the COVID-19 pandemic: a systematic analysis of COVID-19-related mortality, 2020-21. *Lancet (London, England)* **399**, (2022).
3. S. Lopez-Leon *et al.*, More than 50 long-term effects of COVID-19: a systematic review and meta-analysis. *Scientific reports* **11**, (2021).
4. A. Rose, COVID-19 economic impacts in perspective: A comparison to recent U.S. disasters. *International Journal of Disaster Risk Reduction* **60**, (2021).
5. J. Ioannidis, The end of the COVID-19 pandemic. *European journal of clinical investigation* **52**, (2022).
6. L. Gralinski, V. Menachery, Return of the Coronavirus: 2019-nCoV. *Viruses* **12**, (2020).
7. H. Riski, T. Hovi, Coronavirus infections of man associated with diseases other than the common cold. *J Med Virol* **6**, 259-265 (1980).
8. K. McIntosh, Coronaviruses: A Comparative Review. *Current Topics in Microbiology and Immunology* **63**, (1974).
9. C. Wang, P. Horby, F. Hayden, G. Gao, A novel coronavirus outbreak of global health concern. *Lancet (London, England)* **395**, (2020).
10. P. Zhou *et al.*, A pneumonia outbreak associated with a new coronavirus of probable bat origin. *Nature* **579**, (2020).
11. D. Low, A. McGeer, SARS--one year later. *The New England journal of medicine* **349**, (2003).
12. W. Li *et al.*, Bats are natural reservoirs of SARS-like coronaviruses. *Science (New York, N.Y.)* **310**, (2005).
13. X. Ge *et al.*, Isolation and characterization of a bat SARS-like coronavirus that uses the ACE2 receptor. *Nature* **503**, (2013).
14. V. D. Menachery *et al.*, A SARS-like cluster of circulating bat coronaviruses shows potential for human emergence. *Nat Med* **21**, 1508-1513 (2015).
15. Y. Guan *et al.*, Isolation and characterization of viruses related to the SARS coronavirus from animals in southern China. *Science (New York, N.Y.)* **302**, (2003).
16. World Health Organization, Consensus document on the epidemiology of severe acute respiratory syndrome (SARS). (2003).
17. R. Graham, E. Donaldson, R. Baric, A decade after SARS: strategies for controlling emerging coronaviruses. *Nature reviews. Microbiology* **11**, (2013).

18. Johns Hopkins Coronavirus Resource Center, COVID-19 Dashboard - Accessed 2022-10-25. *https://coronavirus.jhu.edu/map.html*, (2022).

19. J. Peiris, K. Yuen, A. Osterhaus, K. Stöhr, The severe acute respiratory syndrome. *The New England journal of medicine* **349**, (2003).

20. D. Oran, E. Topol, Prevalence of Asymptomatic SARS-CoV-2 Infection : A Narrative Review. *Annals of internal medicine* **173**, (2020).

21. K. Lokugamage *et al.*, Type I Interferon Susceptibility Distinguishes SARS-CoV-2 from SARS-CoV. *Journal of virology* **94**, (2020).

22. N. Redondo, S. Zaldívar-López, J. Garrido, M. Montoya, SARS-CoV-2 Accessory Proteins in Viral Pathogenesis: Knowns and Unknowns. *Frontiers in immunology* **12**, (2021).

23. M. Lamers, B. Haagmans, SARS-CoV-2 pathogenesis. *Nature reviews. Microbiology* **20**, (2022).

24. World Health Organization, MERS situtation update, August 2022. (2022).

25. A. Zumla, D. S. Hui, S. Perlman, Middle East respiratory syndrome. *Lancet* **386**, 995-1007 (2015).

26. E. I. Azhar *et al.*, Evidence for camel-to-human transmission of MERS coronavirus. *N Engl J Med* **370**, 2499-2505 (2014).

27. A. N. Alagaili *et al.*, Middle East respiratory syndrome coronavirus infection in dromedary camels in Saudi Arabia. *MBio* **5**, e00884-00814 (2014).

28. S. J. Anthony *et al.*, Further Evidence for Bats as the Evolutionary Source of Middle East Respiratory Syndrome Coronavirus. *MBio* **8**, (2017).

29. M. Oh *et al.*, Middle East respiratory syndrome: what we learned from the 2015 outbreak in the Republic of Korea. *The Korean journal of internal medicine* **33**, (2018).

30. S. Amor, L. Fernández Blanco, D. Baker, Innate immunity during SARS-CoV-2: evasion strategies and activation trigger hypoxia and vascular damage. *Clinical and experimental immunology* **202**, (2020).

31. A. Park, A. Iwasaki, Type I and Type III Interferons - Induction, Signaling, Evasion, and Application to Combat COVID-19. *Cell host & microbe* **27**, (2020).

32. X. Lei *et al.*, Activation and evasion of type I interferon responses by SARS-CoV-2. *Nature communications* **11**, (2020).

33. H. Xia *et al.*, Evasion of Type I Interferon by SARS-CoV-2. *Cell reports* **33**, (2020).

34. D. Gordon *et al.*, A SARS-CoV-2 protein interaction map reveals targets for drug repurposing. *Nature* **583**, (2020).

35. C. Yuen *et al.*, SARS-CoV-2 nsp13, nsp14, nsp15 and orf6 function as potent interferon antagonists. *Emerging microbes & infections* **9**, (2020).

36. A. Stukalov *et al.*, Multilevel proteomics reveals host perturbations by SARS-CoV-2 and SARS-CoV. *Nature* **594**, (2021).

37. X. Xie *et al.*, An Infectious cDNA Clone of SARS-CoV-2. *Cell host & microbe* **27**, (2020).

38. Y. Hou *et al.*, SARS-CoV-2 Reverse Genetics Reveals a Variable Infection Gradient in the Respiratory Tract. *Cell* **182**, (2020).

39. S. Rihn *et al.*, A plasmid DNA-launched SARS-CoV-2 reverse genetics system and coronavirus toolkit for COVID-19 research. *PLoS biology* **19**, (2021).

40. C. Ye *et al.*, Rescue of SARS-CoV-2 from a Single Bacterial Artificial Chromosome. *mBio* **11**, (2020).

41. T. Thi Nhu Thao *et al.*, Rapid reconstruction of SARS-CoV-2 using a synthetic genomics platform. *Nature* **582**, (2020).

42. J. Plante *et al.*, Spike mutation D614G alters SARS-CoV-2 fitness. *Nature* **592**, (2021).

43. B. Johnson *et al.*, Loss of furin cleavage site attenuates SARS-CoV-2 pathogenesis. *Nature* **591**, (2021).

44. M. Vu *et al.*, QTQTN motif upstream of the furin-cleavage site plays a key role in SARS-CoV-2 infection and pathogenesis. *Proceedings of the National Academy of Sciences of the United States of America* **119**, (2022).

45. B. Johnson *et al.*, Nucleocapsid mutations in SARS-CoV-2 augment replication and pathogenesis. *PLoS pathogens* **18**, (2022).

46. Y. Liu *et al.*, The N501Y spike substitution enhances SARS-CoV-2 infection and transmission. *Nature* **602**, (2022).

47. V. D. Menachery *et al.*, Attenuation and restoration of severe acute respiratory syndrome coronavirus mutant lacking 2'-o-methyltransferase activity. *J Virol* **88**, 4251-4264 (2014).

48. V. D. Menachery *et al.*, Middle East Respiratory Syndrome Coronavirus Nonstructural Protein 16 Is Necessary for Interferon Resistance and Viral Pathogenesis. *mSphere* **2**, (2017).

49. S. Daffis *et al.*, 2'-O methylation of the viral mRNA cap evades host restriction by IFIT family members. *Nature* **468**, (2010).

50. R. Züst *et al.*, Ribose 2'-O-methylation provides a molecular signature for the distinction of self and non-self mRNA dependent on the RNA sensor Mda5. *Nature immunology* **12**, (2011).

51. P. V'kovski, A. Kratzel, S. Steiner, H. Stalder, V. Thiel, Coronavirus biology and replication: implications for SARS-CoV-2. *Nature reviews. Microbiology* **19**, (2021).

52. J. Evans, S. Liu, Role of host factors in SARS-CoV-2 entry. *The Journal of biological chemistry* **297**, (2021).

53. M. Romano, A. Ruggiero, F. Squeglia, G. Maga, R. Berisio, A Structural View of SARS-CoV-2 RNA Replication Machinery: RNA Synthesis, Proofreading and Final Capping. *Cells* **9**, (2020).

54. V. Horova *et al.*, Localization of SARS-CoV-2 Capping Enzymes Revealed by an Antibody against the nsp10 Subunit. *Viruses* **13**, (2021).

55. S. Klein *et al.*, SARS-CoV-2 structure and replication characterized by in situ cryo-electron tomography. *Nature communications* **11**, (2020).

56. E. J. Snijder, E. Decroly, J. Ziebuhr, The Nonstructural Proteins Directing Coronavirus RNA Synthesis and Processing. *Adv Virus Res* **96**, 59-126 (2016).

57. E. Snijder, M. Kikkert, Y. Fang, Arterivirus molecular biology and pathogenesis. *The Journal of general virology* **94**, (2013).

58. M. Denison, R. Graham, E. Donaldson, L. Eckerle, R. Baric, Coronaviruses: an RNA proofreading machine regulates replication fidelity and diversity. *RNA biology* **8**, (2011).

59. C. Lauber *et al.*, The footprint of genome architecture in the largest genome expansion in RNA viruses. *PLoS pathogens* **9**, (2013).

60. T. Viswanathan *et al.*, Structural basis of RNA cap modification by SARS-CoV-2. *Nature communications* **11**, (2020).

61. R. Benoni *et al.*, Substrate Specificity of SARS-CoV-2 Nsp10-Nsp16 Methyltransferase. *Viruses* **13**, (2021).

62. M. Bouvet *et al.*, In vitro reconstitution of SARS-coronavirus mRNA cap methylation. *PLoS pathogens* **6**, (2010).

63. A. Walker *et al.*, The SARS-CoV-2 RNA polymerase is a viral RNA capping enzyme. *Nucleic acids research* **49**, (2021).

64. G. Park *et al.*, The mechanism of RNA capping by SARS-CoV-2. *Nature* **609**, (2022).

65. K. Ivanov, J. Ziebuhr, Human coronavirus 229E nonstructural protein 13: characterization of duplex-unwinding, nucleoside triphosphatase, and RNA 5'-triphosphatase activities. *Journal of virology* **78**, (2004).

66. Y. Chen *et al.*, Functional screen reveals SARS coronavirus nonstructural protein nsp14 as a novel cap N7 methyltransferase. *Proceedings of the National Academy of Sciences of the United States of America* **106**, (2009).

67. E. Decroly *et al.*, Coronavirus nonstructural protein 16 is a cap-0 binding enzyme possessing (nucleoside-2'O)-methyltransferase activity. *Journal of virology* **82**, (2008).

68. H. Dong, B. Zhang, P. Shi, Flavivirus methyltransferase: a novel antiviral target. *Antiviral research* **80**, (2008).

69. M. Ringeard, V. Marchand, E. Decroly, Y. Motorin, Y. Bennasser, FTSJ3 is an RNA 2'-O-methyltransferase recruited by HIV to avoid innate immune sensing. *Nature* **565**, (2019).

70. J. Reguera *et al.*, Comparative Structural and Functional Analysis of Bunyavirus and Arenavirus Cap-Snatching Endonucleases. *PLoS pathogens* **12**, (2016).

71. T. Noshi *et al.*, In vitro characterization of baloxavir acid, a first-in-class cap-dependent endonuclease inhibitor of the influenza virus polymerase PA subunit. *Antiviral research* **160**, (2018).

72. Y. Jiang *et al.*, Structural analysis, virtual screening and molecular simulation to identify potential inhibitors targeting 2'-O-ribose methyltransferase of SARS-CoV-2 coronavirus. *Journal of biomolecular structure & dynamics*, (2020).

73. S. Akira, S. Uematsu, O. Takeuchi, Pathogen recognition and innate immunity. *Cell* **124**, (2006).

74. K. Hopfner, V. Hornung, Molecular mechanisms and cellular functions of cGAS-STING signalling. *Nature reviews. Molecular cell biology* **21**, (2020).

75. M. Frieman, M. Heise, R. Baric, SARS coronavirus and innate immunity. *Virus Res* **133**, 101-112 (2008).

76. K. Eisenächer, A. Krug, Regulation of RLR-mediated innate immune signaling--it is all about keeping the balance. *European journal of cell biology* **91**, (2012).

77. Y. Nan, G. Nan, Y. Zhang, Interferon induction by RNA viruses and antagonism by viral pathogens. *Viruses* **6**, (2014).

78. N. Grandvaux *et al.*, Transcriptional profiling of interferon regulatory factor 3 target genes: direct involvement in the regulation of interferon-stimulated genes. *Journal of virology* **76**, (2002).

79. H. Lazear, J. Schoggins, M. Diamond, Shared and Distinct Functions of Type I and Type III Interferons. *Immunity* **50**, (2019).

80. M. Stanifer, K. Pervolaraki, S. Boulant, Differential Regulation of Type I and Type III Interferon Signaling. *International journal of molecular sciences* **20**, (2019).

81. K. Taylor, K. Mossman, Recent advances in understanding viral evasion of type I interferon. *Immunology* **138**, (2013).

82. A. M. Mielech, Y. Chen, A. D. Mesecar, S. C. Baker, Nidovirus papain-like proteases: multifunctional enzymes with protease, deubiquitinating and deISGylating activities. *Virus Res* **194**, 184-190 (2014).

83. J. Thornbrough *et al.*, Middle East Respiratory Syndrome Coronavirus NS4b Protein Inhibits Host RNase L Activation. *mBio* **7**, (2016).

84. H. Mears, T. Sweeney, Better together: the role of IFIT protein-protein interactions in the antiviral response. *The Journal of general virology* **99**, (2018).

85. P. Kumar *et al.*, Inhibition of translation by IFIT family members is determined by their ability to interact selectively with the 5'-terminal regions of cap0-, cap1- and 5'ppp- mRNAs. *Nucleic acids research* **42**, (2014).

86. B. Johnson *et al.*, Human IFIT3 Modulates IFIT1 RNA Binding Specificity and Protein Stability. *Immunity* **48**, (2018).

87. J. Guo, D. Hui, W. Merrick, G. Sen, A new pathway of translational regulation mediated by eukaryotic initiation factor 3. *The EMBO journal* **19**, (2000).

88. G. Williams, N. Gokhale, D. Snider, S. Horner, The mRNA Cap 2'- O-Methyltransferase CMTR1 Regulates the Expression of Certain Interferon-Stimulated Genes. *mSphere* **5**, (2020).

89. M. Stawowczyk, S. Van Scoy, K. Kumar, N. Reich, The interferon stimulated gene 54 promotes apoptosis. *The Journal of biological chemistry* **286**, (2011).

90. S. Xiao *et al.*, RIG-G as a key mediator of the antiproliferative activity of interferon-related pathways through enhancing p21 and p27 proteins. *Proceedings of the National Academy of Sciences of the United States of America* **103**, (2006).

91. Y. Li *et al.*, ISG56 is a negative-feedback regulator of virus-triggered signaling and cellular antiviral response. *Proceedings of the National Academy of Sciences of the United States of America* **106**, (2009).

92. X. Liu, W. Chen, B. Wei, Y. Shan, C. Wang, IFN-induced TPR protein IFIT3 potentiates antiviral signaling by bridging MAVS and TBK1. *Journal of immunology (Baltimore, Md. : 1950)* **187**, (2011).

93. M. Habjan *et al.*, Sequestration by IFIT1 impairs translation of 2'O-unmethylated capped RNA. *PLoS pathogens* **9**, (2013).

94. V. Hornung *et al.*, 5'-Triphosphate RNA is the ligand for RIG-I. *Science (New York, N.Y.)* **314**, (2006).

95. S. Devarkar *et al.*, Structural basis for m7G recognition and 2'-O-methyl discrimination in capped RNAs by the innate immune receptor RIG-I. *Proceedings of the National Academy of Sciences of the United States of America* **113**, (2016).

96. C. Schuberth-Wagner *et al.*, A Conserved Histidine in the RNA Sensor RIG-I Controls Immune Tolerance to N1-2'O-Methylated Self RNA. *Immunity* **43**, (2015).

97. N. Sampaio *et al.*, The RNA sensor MDA5 detects SARS-CoV-2 infection. *Scientific reports* **11**, (2021).

98. X. Yin *et al.*, MDA5 Governs the Innate Immune Response to SARS-CoV-2 in Lung Epithelial Cells. *Cell reports* **34**, (2021).

99. A. Rebendenne *et al.*, SARS-CoV-2 triggers an MDA-5-dependent interferon response which is unable to control replication in lung epithelial cells. *Journal of virology* **95**, (2021).

100. M. Tay, S. Vasudevan, The Transactions of NS3 and NS5 in Flaviviral RNA Replication. *Advances in experimental medicine and biology* **1062**, (2018).

101. M. Issur *et al.*, The flavivirus NS5 protein is a true RNA guanylyltransferase that catalyzes a two-step reaction to form the RNA cap structure. *RNA (New York, N.Y.)* **15**, (2009).

102. M. Byszewska, M. Śmietański, E. Purta, J. Bujnicki, RNA methyltransferases involved in 5' cap biosynthesis. *RNA biology* **11**, (2014).

103. M. Egloff, D. Benarroch, B. Selisko, J. Romette, B. Canard, An RNA cap (nucleoside-2'-O-)-methyltransferase in the flavivirus RNA polymerase NS5: crystal structure and functional characterization. *The EMBO journal* **21**, (2002).

104. D. Ray *et al.*, West Nile virus 5'-cap structure is formed by sequential guanine N-7 and ribose 2'-O methylations by nonstructural protein 5. *Journal of virology* **80**, (2006).

105. Y. Zhou *et al.*, Structure and function of flavivirus NS5 methyltransferase. *Journal of virology* **81**, (2007).

106. J. Kaiser *et al.*, Genotypic and phenotypic characterization of West Nile virus NS5 methyltransferase mutants. *Vaccine* **37**, (2019).

107. J. Li, E. Fontaine-Rodriguez, S. Whelan, Amino acid residues within conserved domain VI of the vesicular stomatitis virus large polymerase protein essential for mRNA cap methyltransferase activity. *Journal of virology* **79**, (2005).

108. Y. Zhang *et al.*, Rational design of human metapneumovirus live attenuated vaccine candidates by inhibiting viral mRNA cap methyltransferase. *Journal of virology* **88**, (2014).

109. C. Valle *et al.*, First insights into the structural features of Ebola virus methyltransferase activities. *Nucleic acids research* **49**, (2021).

110. M. Stewart, P. Roy, Structure-based identification of functional residues in the nucleoside-2'-O-methylase domain of Bluetongue virus VP4 capping enzyme. *FEBS open bio* **5**, (2015).

111. B. Schnierle, P. Gershon, B. Moss, Cap-specific mRNA (nucleoside-O2'-)-methyltransferase and poly(A) polymerase stimulatory activities of vaccinia virus are mediated by a single protein. *Proceedings of the National Academy of Sciences of the United States of America* **89**, (1992).

112. G. Sutton, J. Grimes, D. Stuart, P. Roy, Bluetongue virus VP4 is an RNA-capping assembly line. *Nature structural & molecular biology* **14**, (2007).

113. M. Rosas-Lemus *et al.*, High-resolution structures of the SARS-CoV-2 2'- O-methyltransferase reveal strategies for structure-based inhibitor design. *Science signaling* **13**, (2020).

114. X. Xie *et al.*, Engineering SARS-CoV-2 using a reverse genetic system. *Nature protocols* **16**, (2021).

115. M. Sasaki *et al.*, SARS-CoV-2 variants with mutations at the S1/S2 cleavage site are generated in vitro during propagation in TMPRSS2-deficient cells. *PLoS pathogens* **17**, (2021).

116. G. Katibah *et al.*, tRNA binding, structure, and localization of the human interferon-induced protein IFIT5. *Molecular cell* **49**, (2013).

117. F. Almazán *et al.*, Construction of a severe acute respiratory syndrome coronavirus infectious cDNA clone and a replicon to study coronavirus RNA synthesis. *Journal of virology* **80**, (2006).

118. V. Bergant *et al.*, Attenuation of SARS-CoV-2 replication and associated inflammation by concomitant targeting of viral and host cap 2'-O-ribose methyltransferases. *The EMBO journal* **41**, (2022).

119. M. Imai *et al.*, Syrian hamsters as a small animal model for SARS-CoV-2 infection and countermeasure development. *Proceedings of the National Academy of Sciences of the United States of America* **117**, (2020).

120. V. Menachery, K. Debbink, R. Baric, Coronavirus non-structural protein 16: evasion, attenuation, and possible treatments. *Virus research* **194**, (2014).

121. V. Fensterl, G. Sen, Interferon-induced Ifit proteins: their role in viral pathogenesis. *Journal of virology* **89**, (2015).

122. G. Feng, K. Chong, A. Kumar, B. Williams, Identification of double-stranded RNA-binding domains in the interferon-induced double-stranded RNA-activated p68 kinase. *Proceedings of the National Academy of Sciences of the United States of America* **89**, (1992).

123. J. Donovan, M. Dufner, A. Korennykh, Structural basis for cytosolic double-stranded RNA surveillance by human oligoadenylate synthetase 1. *Proceedings of the National Academy of Sciences of the United States of America* **110**, (2013).

124. M. Diamond, M. Farzan, The broad-spectrum antiviral functions of IFIT and IFITM proteins. *Nature reviews. Immunology* **13**, (2013).

125. C. Pugh, R. Borchardt, H. Stone, Sinefungin, a potent inhibitor of virion mRNA(guanine-7-)-methyltransferase, mRNA(nucleoside-2'-)-methyltransferase, and viral multiplication. *The Journal of biological chemistry* **253**, (1978).

126. P. Krafcikova, J. Silhan, R. Nencka, E. Boura, Structural analysis of the SARS-CoV-2 methyltransferase complex involved in RNA cap creation bound to sinefungin. *Nature communications* **11**, (2020).

127. K. Devkota *et al.*, Probing the SAM Binding Site of SARS-CoV-2 Nsp14 In Vitro Using SAM Competitive Inhibitors Guides Developing Selective Bisubstrate Inhibitors. *SLAS discovery : advancing life sciences R & D* **26**, (2021).

128. E. Sallard, F. Lescure, Y. Yazdanpanah, F. Mentre, N. Peiffer-Smadja, Type 1 interferons as a potential treatment against COVID-19. *Antiviral research* **178**, (2020).

129. Z. Ye *et al.*, Intranasal administration of a single dose of a candidate live attenuated vaccine derived from an NSP16-deficient SARS-CoV-2 strain confers sterilizing immunity in animals. *Cellular & molecular immunology* **19**, (2022).

130. A. Russ *et al.*, Nsp16 shields SARS-CoV-2 from efficient MDA5 sensing and IFIT1-mediated restriction. *EMBO reports*, (2022).

131. Y. Abbas *et al.*, Structure of human IFIT1 with capped RNA reveals adaptable mRNA binding and mechanisms for sensing N1 and N2 ribose 2'-O methylations. *Proceedings of the National Academy of Sciences of the United States of America* **114**, (2017).

132. M. Daugherty, A. Schaller, A. Geballe, H. Malik, Evolution-guided functional analyses reveal diverse antiviral specificities encoded by IFIT1 genes in mammals. *eLife* **5**, (2016).

133. T. Sheahan *et al.*, An orally bioavailable broad-spectrum antiviral inhibits SARS-CoV-2 in human airway epithelial cell cultures and multiple coronaviruses in mice. *Science translational medicine* **12**, (2020).

134. S. Samrat *et al.*, Allosteric inhibitors of the main protease of SARS-CoV-2. *Antiviral research* **205**, (2022).

135. A. Edwards, R. Baric, E. Saphire, J. Ulmer, Stopping pandemics before they start: Lessons learned from SARS-CoV-2. *Science (New York, N.Y.)* **375**, (2022).

136. B. Boras *et al.*, Preclinical characterization of an intravenous coronavirus 3CL protease inhibitor for the potential treatment of COVID19. *Nature communications* **12**, (2021).

137. M. Klima *et al.*, Crystal structure of SARS-CoV-2 nsp10-nsp16 in complex with small molecule inhibitors, SS148 and WZ16. *Protein science : a publication of the Protein Society* **31**, (2022).

138. T. P. Sheahan *et al.*, Broad-spectrum antiviral GS-5734 inhibits both epidemic and zoonotic coronaviruses. *Sci Transl Med* **9**, (2017).

139. R. Hoffman *et al.*, Discovery of Ketone-Based Covalent Inhibitors of Coronavirus 3CL Proteases for the Potential Therapeutic Treatment of COVID-19. *Journal of medicinal chemistry* **63**, (2020).

140. L. Martin, M. Hutchens, C. Hawkins, A. Radnov, How much do clinical trials cost? *Nature reviews. Drug discovery* **16**, (2017).

141. M. Podvinec *et al.*, Novel inhibitors of dengue virus methyltransferase: discovery by in vitro-driven virtual screening on a desktop computer grid. *Journal of medicinal chemistry* **53**, (2010).

142. Y. Khalili, A *et al.*, A High-Throughput Radioactivity-Based Assay for Screening SARS-CoV-2 nsp10-nsp16 Complex. *SLAS discovery : advancing life sciences R & D* **26**, (2021).

143. T. Haline-Vaz, T. Silva, N. Zanchin, The human interferon-regulated ISG95 protein interacts with RNA polymerase II and shows methyltransferase activity. *Biochemical and biophysical research communications* **372**, (2008).

144. T. Otava *et al.*, The Structure-Based Design of SARS-CoV-2 nsp14 Methyltransferase Ligands Yields Nanomolar Inhibitors. *ACS infectious diseases* **7**, (2021).

145. R. Glazer *et al.*, 3-Deazaneplanocin: a new and potent inhibitor of S-adenosylhomocysteine hydrolase and its effects on human promyelocytic leukemia cell line HL-60. *Biochemical and biophysical research communications* **135**, (1986).

146. R. Kumar *et al.*, S-adenosylmethionine-dependent methyltransferase inhibitor DZNep blocks transcription and translation of SARS-CoV-2 genome with a low tendency to select for drug-resistant viral variants. *Antiviral research* **197**, (2022).

147. D. Zhou *et al.*, Robust SARS-CoV-2 infection in nasal turbinates after treatment with systemic neutralizing antibodies. *Cell host & microbe* **29**, (2021).

148. Y. Chen *et al.*, Biochemical and structural insights into the mechanisms of SARS coronavirus RNA ribose 2'-O-methylation by nsp16/nsp10 protein complex. *PLoS pathogens* **7**, (2011).

149. Y. Wang *et al.*, Coronavirus nsp10/nsp16 Methyltransferase Can Be Targeted by nsp10-Derived Peptide In Vitro and In Vivo To Reduce Replication and Pathogenesis. *Journal of virology* **89**, (2015).

150. Y. Liu *et al.*, A live-attenuated SARS-CoV-2 vaccine candidate with accessory protein deletions. *Nature communications* **13**, (2022).

151. V. Menachery *et al.*, Combination Attenuation Offers Strategy for Live Attenuated Coronavirus Vaccines. *Journal of virology* **92**, (2018).

152. R. L. Graham *et al.*, A live, impaired-fidelity coronavirus vaccine protects in an aged, immunocompromised mouse model of lethal disease. *Nat Med* **18**, 1820-1826 (2012).

153. A. Banerjee *et al.*, SARS-CoV-2 Disrupts Splicing, Translation, and Protein Trafficking to Suppress Host Defenses. *Cell*, (2020).

154. J. Hsu, M. Laurent-Rolle, J. Pawlak, C. Wilen, P. Cresswell, Translational shutdown and evasion of the innate immune response by SARS-CoV-2 NSP14 protein. *Proceedings of the National Academy of Sciences of the United States of America* **118**, (2021).

155. A. Matsuda *et al.*, Despite the odds: formation of the SARS-CoV-2 methylation complex. (2022).

156. R. Hernandez, D. Brown, Growth and maintenance of baby hamster kidney (BHK) cells. *Current protocols in microbiology* **Chapter 4**, (2010).

157. E. Winkler *et al.*, SARS-CoV-2 infection of human ACE2-transgenic mice causes severe lung inflammation and impaired function. *Nature immunology* **21**, (2020).

Vita

Craig Daniel Schindewolf was born May 28, 1987 to Deborah Ann Schindewolf and Richard Alton Schindewolf. He received an *Artium Baccalaureus* degree at Princeton University in June, 2009, concentrating in molecular biology. He wrote his senior thesis on modelling the trajectories of foraging *Dictyostelium* amoebae. He received a Master of Science degree in applied mathematics at New Jersey Institute of Technology in August, 2012. As a master's student, he modeled Hodgkin-Huxley neuronal network dynamics in the entorhinal cortex, which resulted in his co-authorship of one publication.

In August, 2017, he entered the Microbiology and Immunology graduate program at the University of Texas Medical Branch at Galveston (UTMB), where he has been researching determinants of pathogenicity of SARS-CoV-2 in the laboratory of Vineet D. Menachery, PhD. He has contributed data to several research articles on SARS-CoV-2 and co-authored reviews on MERS-CoV vaccine candidates and Oropouche fever. In 2021, he secured $11,000 in competitive funding from the Institute for Human Infections and Immunity at UTMB through a COVID-19 pilot grant program for project-related expenses. He also participated in a field epidemiology research experience in Peru for two weeks during the summer of 2018.

Prior to UTMB, he worked as a research technician for Heather B. Jaspan, MD, PhD, at Seattle Children's Research Institute, in Seattle, WA from December, 2015 to August, 2017. In this role, he researched the microbiome of the female reproductive tract and associations with sexually transmitted infections. He also mentored four high school students working in the laboratory.

Prior to Seattle Children's Research Institute, he worked as a laboratory technician for Gal Haspel, PhD at New Jersey Institute of Technology in Newark, NJ from July, 2013

to November, 2015. In this role, he helped create transgenic *C. elegans* (nematode worm) strains for the study of neuronal activity and worm behavior.

Prior to New Jersey Institute of Technology, he worked as a research assistant for K. Stephen Suh, PhD at Hackensack University Medical Center in Hackensack, NJ from October, 2012 to July, 2013. In this role, he researched breast and ovarian cancer biomarkers for predicting disease onset and outcome. He contributed data to a publication on biomarkers for early ovarian cancer diagnosis. He also mentored two high school students working in the laboratory.

His scientific publications to date are:

- Vu MN, Lokugamage KG, Plante JA, Scharton D, Bailey AO, Sotcheff S, Swetnam DM, Johnson BA, Schindewolf C, Alvarado RE, Crocquet-Valdes PA, Debbink K, Weaver SC, Walker DH, Russell WK, Routh AL, Plante KS, Menachery VD (2022) "QTQTN motif upstream of the furin-cleavage site plays a key role in SARS-CoV-2 infection and pathogenesis." Proceedings of the National Academy of Sciences, 119(32), e2205690119.
- Johnson BA, Zhou Y, Lokugamage KG, Vu MN, Bopp N, Crocquet-Valdes PA, Kalveram B, Schindewolf C, Liu Y, Scharton D, Plante JA, Xie X, Aguilar P, Weaver SC, Shi PY, Walker DH, Routh AL, Plante KS, Menachery VD (2022): "Nucleocapsid mutations in SARS-CoV-2 augment replication and pathogenesis." PLoS Pathogens, 18(6), e1010627.
- Liu Y, Liu J, Johnson BA, Xia H, Ku Z, Schindewolf C, Widen SG, An Z, Weaver SC, Menachery VD, Xie X, Shi PY (2022): "Delta spike P681R mutation enhances SARS-CoV-2 fitness over Alpha variant." Cell Reports, 39(7), 110829.
- Files MA, Hansen CA, Herrera VC, Schindewolf C, Barrett ADT, Beasley DWC, Bourne N, Milligan GN (2022): "Baseline mapping of Oropouche

virology, epidemiology, therapeutics, and vaccine research and development." npj Vaccines, 7(1), 1-10.

- Liu Y, Liu J, Plante KS, Plante JA, Xie X, Zhang X, Ku Z, An Z, Scharton D, Schindewolf C, Widen SG, Menachery VD, Shi PY, Weaver SC (2022): "The N501Y spike substitution enhances SARS-CoV-2 transmission." Nature, 602(7896), 294-299.
- Muruato A, Vu MN, Johnson BA, Davis-Gardner ME, Vanderheiden A, Lokugamage K, Schindewolf C, Crocquet-Valdes PA, Langsjoen RM, Plante JA, Plante KS, Weaver SC, Debbink K, Routh AL, Walker D, Suthar MS, Shi PY, Xie X, Menachery VD (2021): "Mouse-adapted SARS-CoV-2 protects animals from lethal SARS-CoV challenge." PLoS Biology, 19(11), e3001284
- Johnson BA, Xie X, Bailey AL, Kalveram B, Lokugamage KG, Muruato A, Zou J, Zhang X, Juelich T, Smith JK, Zhang L, Bopp N, Schindewolf C, Vu M, Vanderheiden A, Winkler ES, Swetnam D, Plante JA, Aguilar P, Plante KS, Popov V, Lee B, Weaver SC, Suthar MS, Routh AL, Ren P, Ku Z, An Z, Debbink K, Diamond M, Shi PY, Freiberg AN, Menachery VD (2021): "Loss of furin cleavage site attenuates SARS-CoV-2 pathogenesis." Nature, 591(7849), 293-299.
- Lokugamage KG, Hage A, Devries M, Valero-Jimenez A, Schindewolf C, Dittmann M, Rajsbaum R, Menachery VD (2020): "Type I interferon susceptibility distinguishes SARS-CoV-2 from SARS-CoV." Journal of Virology, 94(23), e01410-20.
- Xie X, Muruato A, Lokugamage KG, Narayanan K, Zhang X, Zou J, Liu J, Schindewolf C, Bopp NE, Aguilar PV, Plante KS, Weaver SC, Makino S, LeDuc JW, Menachery VD, and Shi PY (2020): "An Infectious cDNA Clone of SARS-CoV-2." Cell Host & Microbe. 27(5), 841-848.

- Harcourt J, Tamin A, Lu X, Kamili S, Sakthivel SK, Murray J, Queen K, Tao Y, Paden CR, Zhang J, Li Y, Uehara A, Wang H, Goldsmith C, Bullock HA, Wang L, Whitaker B, Lynch B, Gautam R, Schindewolf C, Lokugamage KG, Scharton D, Plante JA, Mirchandani D, Widen SG, Narayanan K, Makino S, Ksiazek TG, Plante KS, Weaver SC, Lindstrom S, Tong S, Menachery VD, and Thornburg NJ (2020): "Severe Acute Respiratory Syndrome Coronavirus 2 From Patient With 2019 Novel Coronavirus Disease, United States." Emerging Infectious Diseases, 26(6), 1266.
- Schindewolf C and Menachery VD (2019): "Middle East respiratory syndrome vaccine candidates: Cautious optimism." Viruses, 11(1), 74.
- Schindewolf C, Kim D, Bel A, Rotstein HG (2016): "Complex patterns in networks of hyperexcitable neurons." Theoretical Computer Science, 633, 71-82.
- Tamir A, Jag U, Sarojini S, Schindewolf C, Tanaka T, Gharbaran R, Patel H, Sood A, Hu W, Patwa R, Blake P, Chirina P, Oh Jeong J, Lim H, Goy A, Pecora A, Suh KS (2014): "Kallikrein family proteases KLK6 and KLK7 are potential early detection and diagnostic biomarkers for serous and papillary serous ovarian cancer subtypes." Journal of Ovarian Research, 7(1), 1-15.

Lastly, he has held various jobs as a data analyst for Teach for America, biotechnology consultant, tutor, office assistant, lifeguard, busboy, server, janitor, and landscaper.

Permanent address: 301 University Blvd, Galveston, TX 77555

This dissertation was typed by Craig Schindewolf.